The Pennsylvania State University

The Graduate School

Eberly College of Science

SYNTHESIS AND CHARACTERIZATION OF SEMICONDUCTOR NANOMATERIALS FOR THERMOELECTRIC APPLICATIONS

A Dissertation in

Chemistry

by

Matthew R. Dirmyer

Submitted in Partial Fulfillment
of the Requirements
for the Degree of

Doctor of Philosophy

August 2009

The dissertation of Matthew R. Dirmyer was reviewed and approved* by the following:

Ayusman Sen
Professor of Chemistry
Head of the Department of Chemistry
Dissertation Advisor
Chair of Committee

John V. Badding
Professor of Chemistry

David L. Allara
Professor of Polymer Science and Chemistry

James Runt
Professor of Polymer Science

*Signatures are on file in the Graduate School

Abstract

In this dissertation, I explore simple chemical means to produce various nanomaterials. In Chapter 2, the synthesis of size-tuned bismuth telluride nanoparticles is discussed. The solution phase synthesis of bismuth telluride nanoparticles has been accomplished in the presence of a library of thiols as the capping ligand. These crystalline nanostructures range in size from ~20 to ~100 nm with a relatively narrow size dispersity. Size and shape of the resulting nanostructures has been investigated as a function of chain length of the thiol and temperature. An investigation into the thermoelectric properties of the nanostructures shows promising electrical conductivity, thermopower, and thermal conductivity for undoped bismuth telluride. In Chapter 3, a soluble precursor for antimony telluride is described. This precursor was used to fabricate semiconductor nanowires of varying diameter and thin films through simple templating methods. Electrical conductivity and thermoelectric power measurements of these films are only slightly lower than for antimony telluride films fabricated by vacuum deposition. In Chapter 4, the polytetrafluoroethylene (PTFE)/metal nanocomposites are discussed. Palladium and nickel PTFE nanocomposites were made by impregnation of the polymer with metal acetates. Annealing and jet blowing of these materials form PTFE nanofiber/metal nanoparticle composites.

Contents

List of Figures

List of Tables

Preface

The work described in this dissertation was carried out between August 2003 and August 2009 under the direction of Dr. Ayusman Sen at the Pennsylvania State University. The body of this work is divided across three projects, which are presented as chapters herein. It should be noted that because of the collaborative nature of projects within Dr. Sen's group, researchers other than myself contributed to the projects presented in the following chapters. The results of these collaborative efforts are included in order to maintain the context and completeness of each project. However, their inclusion should not be construed as a claim of sole-authorship. The division of labor for each project is clarified below.

The research presented in Chapter 2 was initiated by myself and performed in collaboration with the following people as noted in the original publication. Electrical conductivity, thermoelectric power, and carrier concentration measurements were performed in collaboration with Dr. John Badding. Thermal conductivity measurements were performed by Dr. George Nolas and Dr. Joshua Martin of The University of South Florida. X-ray photoelectron spectroscopy was carried out in collaboration with Dr. Jonathan Shu of Cornell University.

The research presented in Chapter 3 was initiated by myself. Electrical conductivity measurements were performed in collaboration with Dr. Rongrui He. 100 nm alumina templates were provided by Dr. James Sioss.

The research presented in Chapter 4 was initiated by Dr. Sachin Borkar with

assistance from myself and Roland Delicado. Synthesis of the PTFE/nickel nanocomposites was carried out by myself. Synthesis of the PTFE/Pd nanocomposites was performed by Dr. Sachin Borkar and Roland Delicado. Jet blowing experiments were carried out by Roland Delicado and myself under the supervision of Dr. Sachin Borkar. Ultrathin cryotomy was carried out by myself with direction from Missy Hazen.

Acknowledgements

As I sit here writing this thesis, I realize it is a culmination of many years of education and hard work that would not be possible without the help of all my teachers, mentors, family, and friends; I merely stand on the shoulders of all these people and am forever indebted for their inspiration and words given to me along this journey.

I am eternally grateful for the guidance and support of my advisor Dr. Ayusman Sen. His support, both financial and intellectual, will never be forgotten. A proper mix of his skepticism and enthusiasm has been excellent motivation throughout my research. It has been a true pleasure and honor to work for Aysuman. Various materials properties measurements would not have been possible without the help of Dr. John Badding: sharing the company of a full professor at two in the morning working on carrier concentration measurements is a testament to his commitment towards his students. His knowledge, constant curiosity, and personality have made graduate school rewarding. I would also like to thank Dr. David Allara and Dr. James Runt for serving on my doctoral committee.

Misery loves company; I am very thankful for my fellow Sen group members with whom I have commiserated over the sheer frustrations and celebrated in the absolute joys of experimental chemistry. In particular, Dr. Walter Paxton, Dr. Sachin Borkar, Dr. Angel Ugrinov, Dr. David Newsham, Michael Ibele, and Betty Jo Houser have all made the bright and dark times brighter with their words of

support and humor, and countless trips downtown for a lunch break at College Pizza. Special thanks to Dr. David Newsham for his help with LaTeX and thesis layout and any other computer problem I've ever had during graduate school.

I would also like to thank my circle of Penn Staters that have helped quell the insanity of graduate school: Dr. Jeffrey Gall, my best friend since high school, has been there for me since the beginning of graduate school; my dear friend, Dr. James Sioss, without whom I can not imagine success in graduate school or Penn State tailgating; Jason and Amy Schatz, whose constant friendship and dedication to "Football Saturdays" in the fall are true examples of what it means to be a Penn Stater; Stacey Dean, my "bf", whose compassion and caring nature made the twilight of my graduate career bearable; and Justin Sparks, whose refreshing attitude towards research and passion for hockey was a welcome break from science.

Finally, I would like to thank my wonderful family for their unwavering support. My mother, Debby, and father, Richard, have given me everything I have needed to survive and succeed in this world. My sister, Michelle, who laid out before me a blueprint of academic success as I followed her through the same school halls. My grandparents, Eugene and Ruth Dirmyer and Robert and Erna Schultz, who are truly all members of "The Greatest Generation" for instilling in me a work ethic forged through true-life experience. Special gratitude to Robert Schultz whose personal approach to problem solving has become an adopted mantra of my own: "It's just like anything else. With the proper knowledge and tools, you can do anything."

Epigraph

"That very night in Max's room a forest grew and grew and grew until his ceiling hung with vines and the walls became the world all around and an ocean tumbled by with a private boat for Max and he sailed off through night and day and in and out of weeks and almost over a year to where the wild things are... 'And now,' cried Max, 'let the wild rumpus start!' "

–Maurice Sendak, Where the Wild Things Are (1963)

Chapter One

Introduction

1.1 Background

Global concerns about the environment have led to intense research into how energy is used and how it could be used more efficiently. Current "green" technologies focus on limiting the amount of ozone depletion, greenhouse gas emission, and fossil fuel usage.[1] Thermoelectric materials may be a viable solution to part of our current global environmental crisis. Thermoelectrics are solid-state materials that are capable of converting electricity into a temperature differential (cooling via the Peltier Effect) or a temperature differential into electricity (Seebeck Effect).[2]

While the poor performance of thermoelectric materials has limited their applications, the commercial market for thermoelectric power generators is estimated to be US$25–50 million per annum and US$200–250 million per annum for thermoelectric cooling systems. Thermoelectrics are used in high-end systems where reliability is more important than efficiency such as power generation in outer space. Examples of commercially available technologies where thermoelectric cooling is used include: laser diode coolers, biological assay thermal cyclers, climate-control seating in automobiles, portable beverage/picnic coolers, mini-refrigerators, and personal cooling devices. In order to make a thermoelectric home heating and cooling system practical, a doubling in the efficiency of the current state-of-the-art materials is necessary.[1]

Another attractive feature of thermoelectric cooling devices is that they are completely solid-state and, therefore, require no working fluid. Although ozone-depleting Freons have been phased out of cooling applications since the early 1990s, its most common replacement, R-134a, is a very harmful greenhouse gas. R-134a will be banned in new European cars by 2011 with a larger scale ban to follow.[3] This creates a need for alternative air conditioning technologies.

Thermoelectric devices can be used to generate a temperature differential or as power generators. A thermoelectric element is composed of a p-type and n-type material. In the case of thermoelectric cooling, a potential is applied to the circuit and it forces the electrons and holes to travel towards the heat sink side of the thermoelectric element. The electrons and holes also carry heat, resulting in cooling (Figure 1.1).[2] The performance of a thermoelectric material is quantified by the dimensionless figure of merit, ZT, which is defined as:

$$ZT = \frac{\sigma S^2}{\kappa} T$$

where σ is the electrical conductivity, S is the thermoelectric power or Seebeck coefficient, κ is the thermal conductivity, and T is the absolute temperature. Therefore, good thermoelectric materials will have a high electrical conductivity and thermoelectric power while possessing a low thermal conductivity. However, each of the properties are interrelated and optimization of one leads to the diminishing of another. Metals are good electrical conductors but also have very high thermal conductivities. Insulators are poor electrical and thermal conductors (Figure 1.2). A compromise must be made; a maximum of σS^2 as a function of carrier concentration is found in the semiconductor region.[4] Therefore, most thermoelectrics are heavily doped semiconductors. Classic semiconductors (Si, Ge) have appropriately high carrier concentrations but also high thermal conductivities. Highly covalent intermetallic compounds composed of heavy elements best satisfy the compromise made in thermoelectrics (Pb, Hg, Tl, Bi, Sb, and S, Se, Te).[5] Figure 1.3 shows a plot of the ZT of various thermoelectric materials as a function of temperature. Heavily doped bismuth telluride and its alloys are the best performing thermoelectric materials at room temperature and are used as thermoelectric heat pumps. This dissertation deals with the nanostructuring of bismuth and antimony tellurides as

a strategy to improve their thermoelectric properties.

In 1993, the Office of Naval Research and Defense Advanced Research Projects began funding for a renewed interest in thermoelectrics research with the general theme of applying the new ideas of nanotechnology to the old problem of optimizing thermoelectric materials. Theoretical studies by Hicks and Dresselhaus suggested nanoengineered materials could achieve enhanced thermoelectric properties.[6] High-ZT nanostructured thermoelectrics have been reported: Venkatasubramian reported a ZT of ~2.4 at room temperature for Bi_2Te_3/Sb_2Te_3 superlattices fabricated by metal-organic chemical vapor deposition,[7] and Harman reported a ZT of ~3.2 at 300°C for PbSeTe/PbTe quantum dot superlattices fabricated by molecular beam epitaxy.[8] While these reports represent great achievements in the field of thermoelectrics, the materials investigated require expensive, low throughput, high vacuum methods. As such, these materials have not yet been integrated into commercial devices.

Quantum confined semiconductors composed of heavy elements hold great promise as thermoelectric materials. An increase in the density of states near the Fermi level due to quantum confinement effects and an increased scattering of boundary phonons due to nanostructuring can lead to an increase in ZT.[6,9] To realize the highest-ZT quantum confined material possible from a conventional thermoelectric semiconductor material such as bismuth telluride, meeting several criteria are important. First, it is reasonable to expect that uniform, optimal size quantum domains will lead to the highest ZT at a given doping level. The electronic structure of the semiconductor, which determines the thermoelectric power, depends on the degree of quantum confinement, and thus the domain size. Second, the interfacial electrical transport must be optimized. The presence of impurities between the domains/particles typically leads to barriers to transport

that reduce the electrical conductivity. Third, while optimizing electrical transport between domains, it is important that the nanostructured architecture not be destroyed, or the phonon scattering will decrease and the thermal conductivity will increase. Fourth, it is well known that proper doping is critical to the performance of bulk thermoelectric materials, and thus quantum confined thermoelectrics must be carefully doped as well.

In this dissertation, practical solutions to the fabrication of nanostructured thermoelectric materials are presented. In Chapter 2, we describe a simple, scalable, solution-based synthetic route to nanostructured bismuth telluride. Nanoparticle dimensions can be tuned by changing reaction parameters such as capping ligand or reaction temperature. Thermoelectric properties measurements on these materials show that nanostructuring is a viable way to increase the ZT of these materials. In Chapter 3, a method for the fabrication of antimony telluride nanowires and thin films is presented. A simple soluble antimony telluride precursor has been synthesized allowing for the tuning of film composition from n-type to p-type semiconductors. Electrical conductivity and thermoelectric power measurements of these films show promising results.

An additional chapter in this dissertation, Chapter 4, is dedicated to the exploration of polytetrafluoroethylene (PTFE)/metal (palladium and iron) nanoparticle composite systems. A simple method for the insitu formation of metallic nanoparticles within a PTFE matrix is described. This composite is then processed through a technique known as jet blowing to produce PTFE micro/nanofibers which are impregnated with iron or palladium nanoparticles.

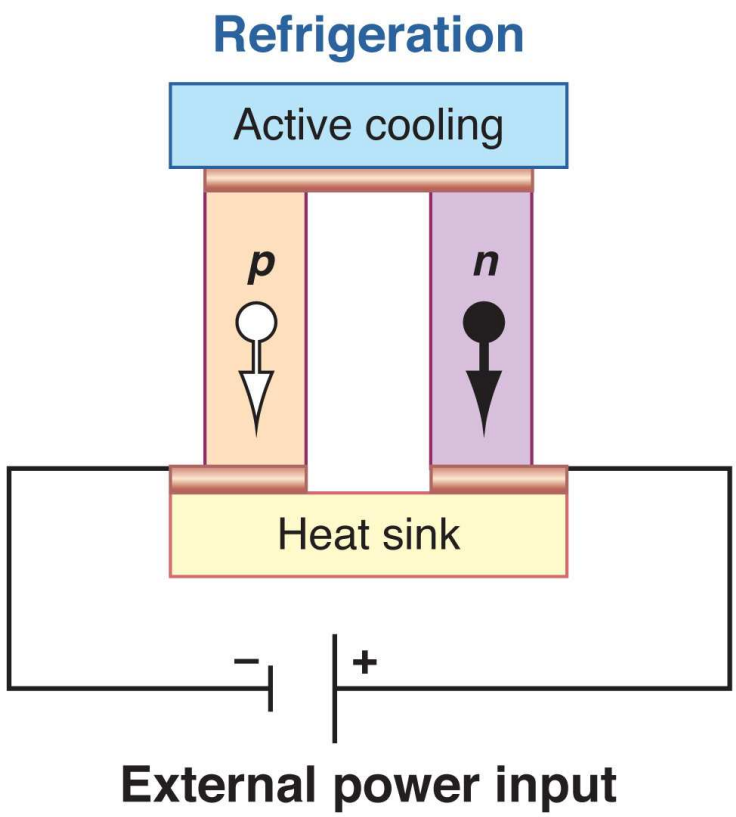

Figure 1.1: A thermoelectric element operating as a heat pump.[2]

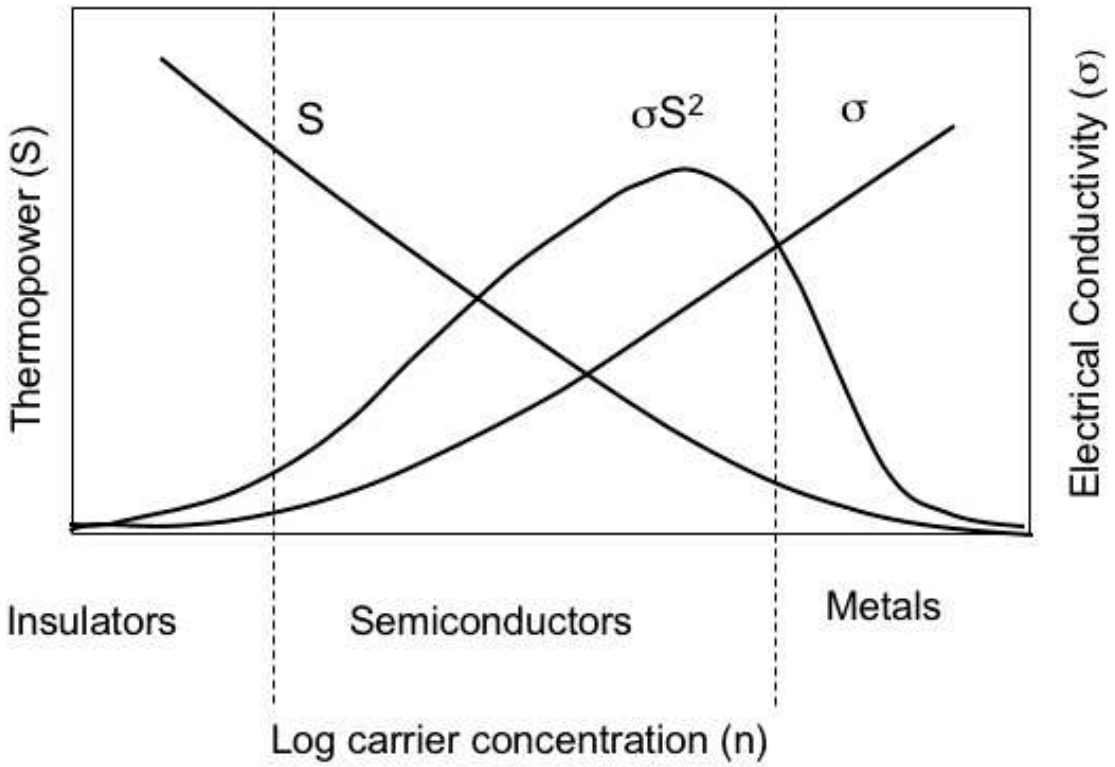

Figure 1.2: Electrical conductivity and thermoelectric power as a function of carrier concentration. [4]

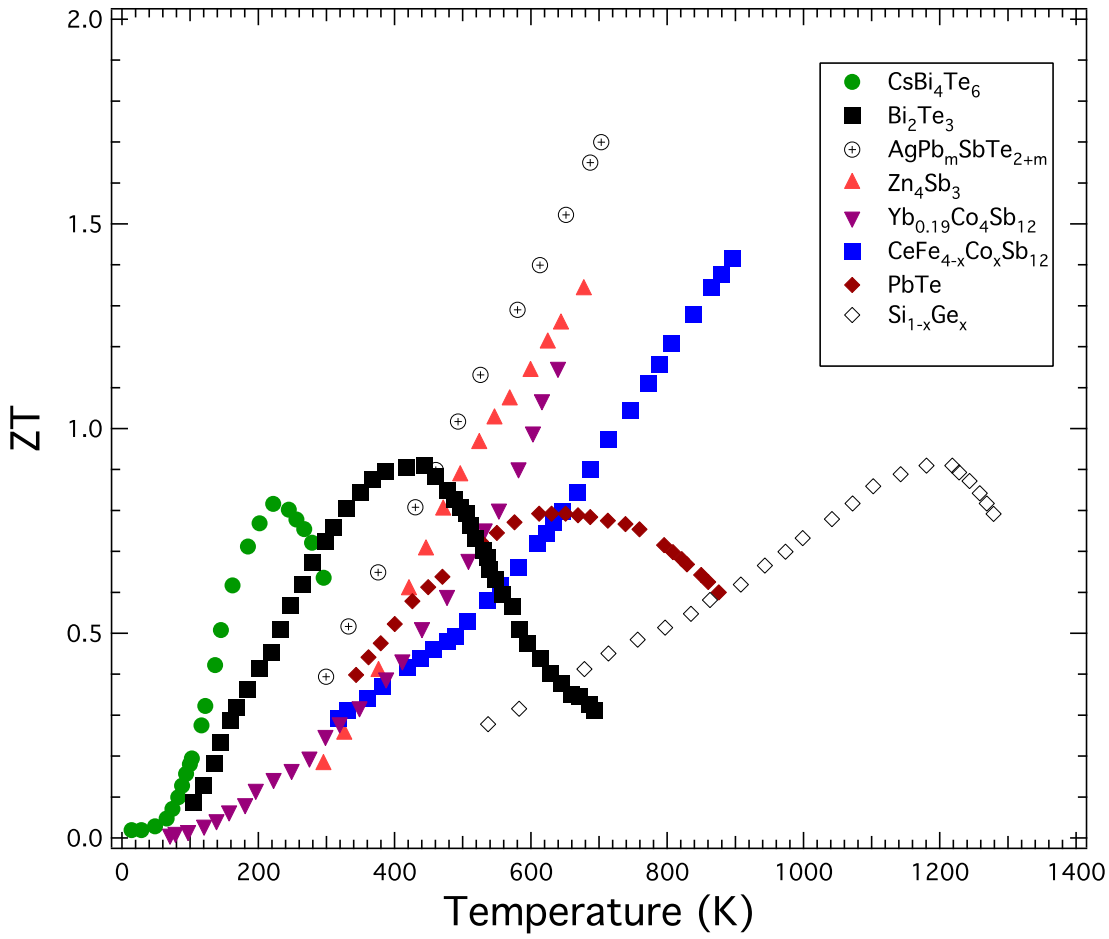

Figure 1.3: ZT as a function of temperature for various thermoelectric materials.[5]

1.2 References

[1] Bell, L. *Science* **2008**, *321*, 1457–1461.

[2] Sales, B. *Science* **2002**, *295*, 1248–1249.

[3] Vining, C. *Nat. Mater.* **2009**, *8*, 83–85.

[4] Mahan, G. *Solid State Physics*; Academic Press, 1998; Vol. 51, p 92.

[5] Tritt, T.; Subramanian, M. *Mat. Res. Soc. Bull.* **2006**, *31*, 188–194.

[6] Hicks, L.; Dresselhaus, M. *Phys. Rev. B.* **1993**, *47*, 16631–16634.

[7] Venkatasubramanian, R.; Siilvola, E.; Colpitts, T.; O'Quinn, B. *Nature* **2001**, *413*, 597–602.

[8] Harman, T.; Taylor, P.; Walsh, M.; LaForge, B. *Science* **2002**, *297*, 2229–2232.

[9] Mahan, G.; Sofo, J. *Proc. Natl. Acad. Sci USA* **1996**, *93*, 7436–7439.

Chapter Two

Synthesis, Characterization, and Thermoelectric Properties of Nanostructured Bismuth Telluride

2.1 Introduction

This chapter describes the solution-phase synthesis and thorough characterization of thiol-capped bismuth telluride single-crystal nanoparticles that range in size from ~17 to ~100 nm with an improved dispersity that is typically 12 to 13%, significantly better than the previously reported values.[1] The chain length of the capping alkane thiol and reaction temperature are used to control the size of the resulting nanostructures. It was observed that it is possible to carefully anneal the particles to drive off the capping agent while maintaining phase purity and then press them into pellets to improve the electrical transport properties. The carrier concentration was determined for the first time for chemically synthesized bismuth telluride via Hall effect measurements. As expected, annealing significantly improves the thermoelectric properties, which are best for the samples prepared with the smallest particle sizes. Thermal conductivity measurements on chemically synthesized and annealed bismuth telluride nanoparticles have not been previously reported, likely due to issues with low sample purity and density. We were able to press our samples to densities of 87% of the bulk density and found that the thermal conductivity can be as much as 2 times lower than that of optimized commercial antimony bismuth telluride alloy and is independent of temperature.[2] Additional advantages of our synthetic method include relative simplicity, short reaction times, and relatively mild reaction conditions.

Nanostructured bismuth telluride has been reported through the electrodeposition in alumina templates,[3,4] solvothermal methods,[5,6] reverse micelle synthesis,[1,7] laser ablation,[8] and precipitation from solvent.[9–11] The resulting nanostructures are usually too large (80–100s of nm) to be quantum confined and suffer from a large size distribution. There are a few reports of chemical synthetic approaches

to sub 80 nm bismuth telluride nanoparticles, but thus far the challenges in assembling them into pure, quantum confined materials with excellent interparticle electrical transport and low thermal conductivity have not been met.[10,12,13] A previous attempt to anneal capped bismuth telluride particles resulted in materials that exhibit diffraction peaks for bismuth telluride sulfide that are approximately two times more intense than for bismuth telluride, indicating that a new majority phase with a different crystal structure is produced due to incorporation of sulfur from the capping agent; this sulfide phase would not be expected to have the superior thermoelectric properties of bismuth telluride. The presence of impurities between the grains leads to non-ohmic electrical transport behavior in annealed thin films.[1] The electrical conductivity of these materials has not been reported, but it is likely not high in view of the non-ohmic behavior.

2.2 Synthesis of Nanostructured Bismuth Telluride

Nanostructured bismuth telluride (n–Bi_2Te_3) was synthesized via simple solution-based chemistry. A key feature of a solution-based synthetic method is versatility; different components such as metal precursor, and capping ligand can be readily modified. The method is outlined in Figure 2.1.

To prepare the bismuth telluride nanoparticles, either octane-, dodecane-, or octadecanethiol was used as a capping ligand to limit particle growth to the nanoscale. Soluble bismuth and tellurium precursors were used in a high-boiling, non-coordinating solvent. The alkane thiol was added to bismuth neodecanoate in diphenyl ether under an inert nitrogen atmosphere. The reaction solution changed color from colorless to a clear, yellow solution. A UV-Vis study of this solution (Figure 2.2) showed a peak at 365 nm, attributable to coordination of the thiol to the Bi^{3+} ion.[14] Trioctylphosphine telluride was then added and a color change from yellow to black was observed. The reaction was carried out for 1 hour at either 50 °C or 150 °C. At the end of this period, the mixture was allowed to cool and the thiol-capped bismuth telluride nanoparticles were collected by centrifugation. The sample labeling convention for nanostructured bismuth telluride here is as follows: n–Bi_2Te_3, number of carbons in the chain for the thiol capping ligand -SH, and synthesis temperature, e.g. n–Bi_2Te_3C18SH50 represents octadecanethiol-capped bismuth telluride synthesized at 50 °C.

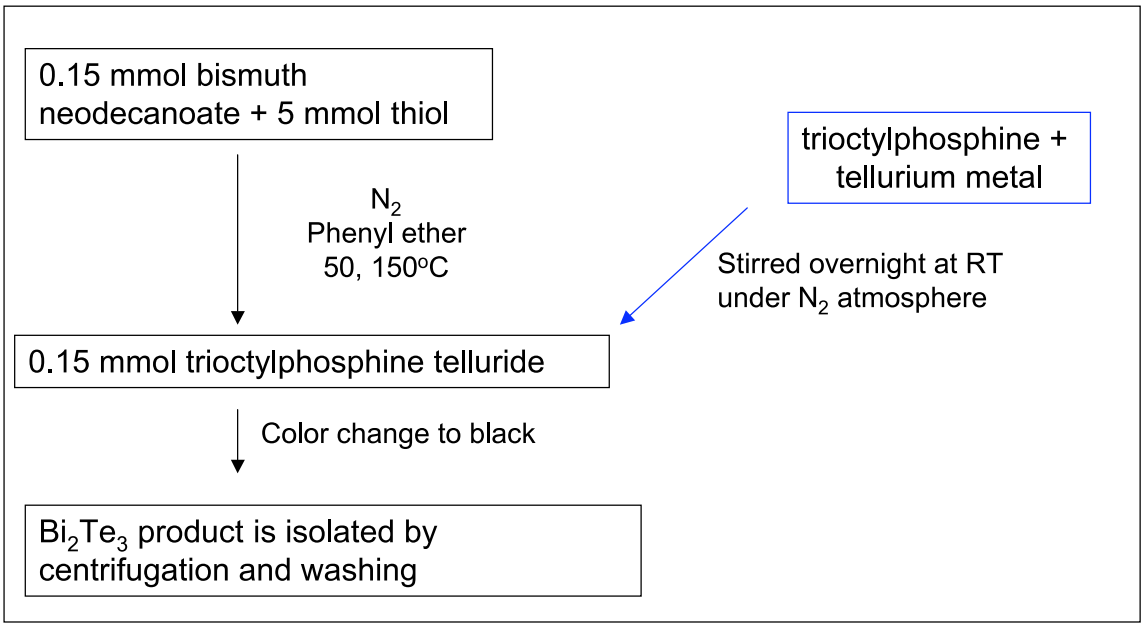

Figure 2.1: Reaction scheme for the synthesis of nanostructured Bi_2Te_3.

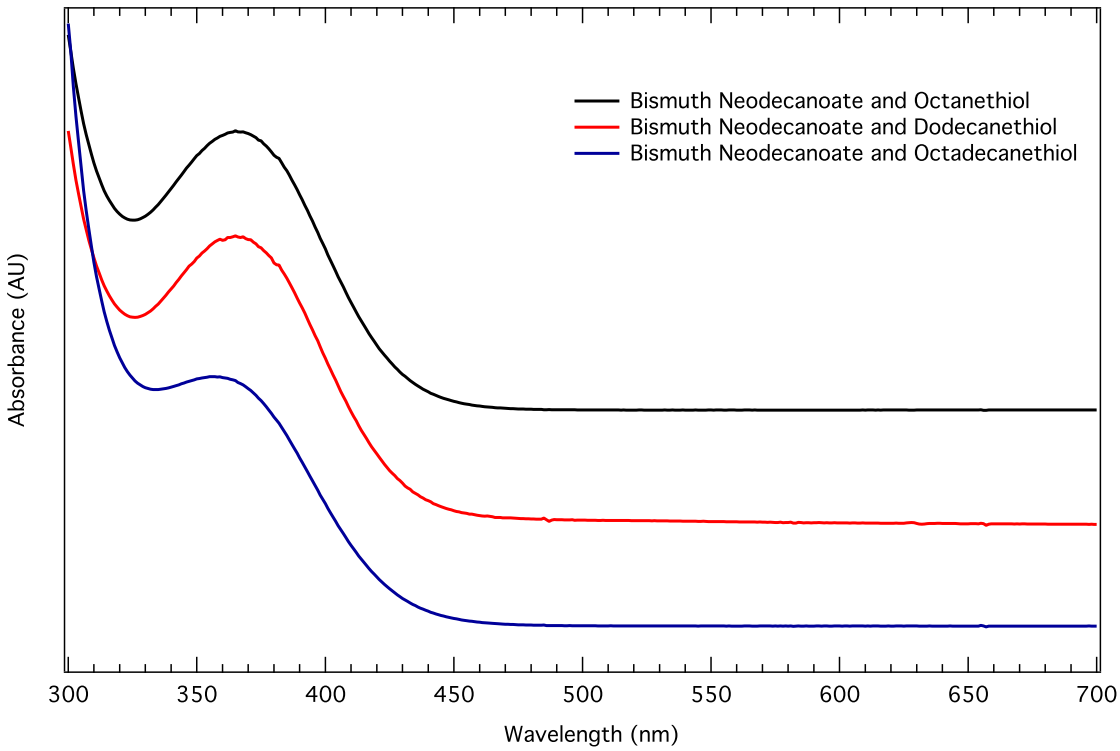

Figure 2.2: UV-Vis spectra of bismuth neodecanoate and various alkanethiols.

2.3 Characterization of Nanostructured Bismuth Telluride

The morphology, phase, surface properties, and thermal properties of the nanostructured bismuth telluride were thoroughly characterized. Transmission electron microscopy (TEM) was used to observe the particles' morphology. Energy dispersive spectroscopy (EDS) was used to determine the composition of the material; while powder X-ray diffraction (XRD) confirms that the material is a nanocrystalline phase of bismuth telluride, which is further confirmed by electron diffraction of single bismuth telluride particles. Nuclear magnetic resonance (NMR) and X-ray photoelectron spectroscopy (XPS) were used to confirm the presence of the thiol capping ligands and a small amount of surface oxide, respectively. Thermal gravimetric analysis (TGA) and differential scanning calorimetry (DSC) were used to characterize the thermal stability of assemblies of the nanostructures.

The morphology of nanostructured bismuth telluride was observed by TEM. Figure 2.3 shows representative TEM micrographs of bismuth telluride nanoparticles synthesized with a variety of thiol capping ligands at 150 °C and 50 °C. The particles are roughly spherical in shape. Average particle size and size distribution of the as-synthesized nanoparticles was determined by analysis of 200 nanoparticles imaged in TEM micrographs. Table 2.1 shows the particle size for nanoparticles synthesized under varying conditions. It was observed that the particle size could be controlled by manipulating two of the reaction conditions: the length of the carbon chain of the thiol capping ligand and reaction temperatures. At a given reaction temperature, particles synthesized with longer alkyl chain thiols produce smaller particles and shorter alkyl chain thiols produce larger particles. The greater steric bulk of the longer alkyl chains shields the newly formed particle more effectively, thus inhibiting its growth. Reactions at 150 °C, while using the

same thiol, produce larger nanoparticles than reactions at 50°C. At higher temperatures particle growth is faster thus producing larger nanoparticles. Electron diffraction patterns of individual capped particles (Figure 2.4) reveal that they are single crystals. In the absence of the capping agent, large irregular structures were formed (Figure 2.5). This confirms the important role the thiol plays as a capping ligand.

Table 2.1: Thermoelectric properties of as-synthesized and annealed nanostructured bismuth telluride. Average particle size, electrical conductivity (σ), thermoelectric power (S), and power factor (σS^2) of the as-synthesized and annealed nanostructured bismuth telluride compared to bulk bismuth telluride.

Sample ID	Average Particle Size ((Std. Dev.) nm)	σ ($\mathrm{S\,cm^{-1}}$)	S ($\mu\mathrm{V\,K^{-1}}$)	Power Factor ($\mu\mathrm{V^2\,cm^{-1}\,K^{-2}}$)
Bulk Bi_2Te_3 (99.99%)		12.2	−125	1.9×10^5
n-Bi_2Te_3C18SH50	17 (2)	1.07×10^{-3}	−49	2.6
n-Bi_2Te_3C18SH50[a]	39 (7)	30.4	−150	6.9×10^5
n-Bi_2Te_3C12SH50	23 (3)	6.23×10^{-5}	−49	1.5×10^{-1}
n-Bi_2Te_3C12SH50[a]	34 (17)	9.49	−191	3.5×10^5
n-Bi_2Te_3C8SH50	29 (5)	5.81×10^{-5}	−49	1.4×10^{-1}
n-Bi_2Te_3C8SH50[a]	60 (12)	49.6	−91	4.1×10^5
n-Bi_2Te_3C12SH150	45 (6)	2.67×10^{-1}	−78	1.6×10^3
n-Bi_2Te_3C12SH150[a]	40 (4)	24.1	−82	1.6×10^5
n-Bi_2Te_3C18SH150	52 (7)	3.50×10^{-1}	−85	2.5×10^3
n-Bi_2Te_3C18SH150[a]	57 (7)	5.89×10^{-1}	−91	4.9×10^3
n-Bi_2Te_3C8SH150	98 (15)	1.24	−69	5.9×10^3
n-Bi_2Te_3C8SH150[a]	86 (9)	6.08	−89	4.8×10^4

[a] post-annealing

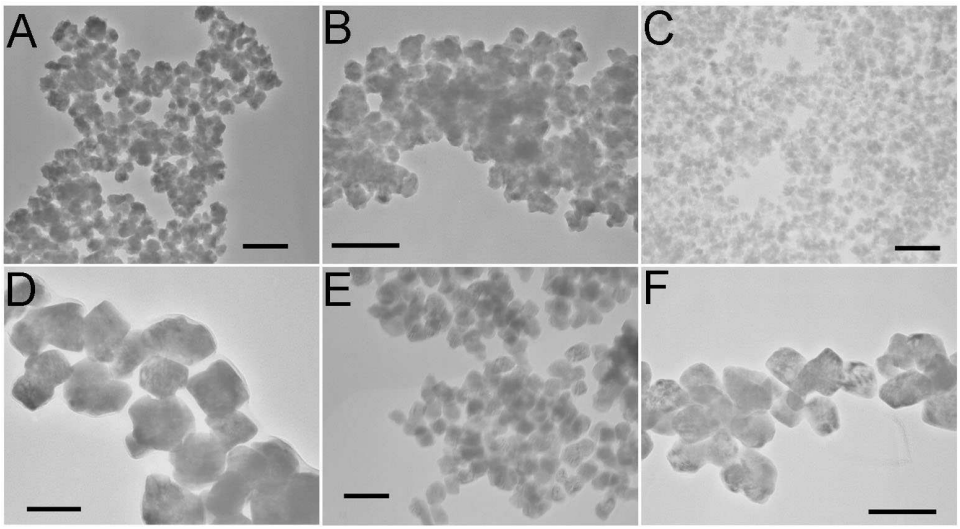

Figure 2.3: TEM images of nanostructured bismuth telluride. A: TEM image of n–Bi_2Te_3C8SH50, B: TEM image of n–Bi_2Te_3C12SH50, C: TEM image of n–Bi_2Te_3-C18H50, D: TEM image of n–Bi_2Te_3C8SH150, E: TEM image of n–Bi_2Te_3C12SH150, and E: TEM image of n–Bi_2Te_3C18SH150. All scale bars are equal to 100 nm.

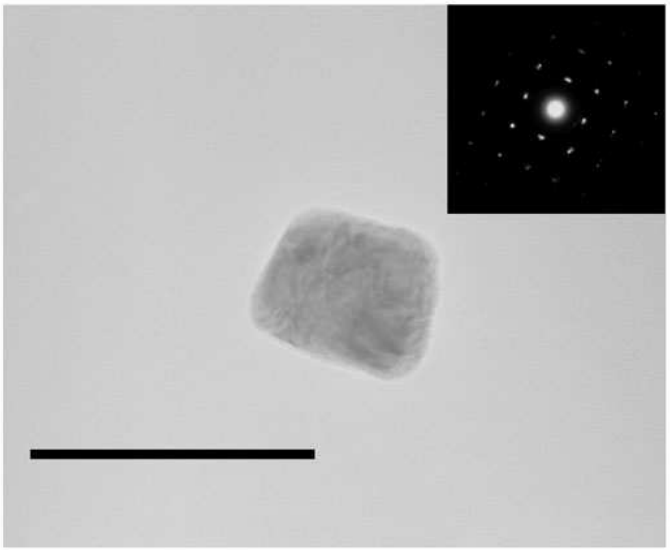

Figure 2.4: TEM image of one n–Bi_2Te_3C18SH150 particle with electron diffraction inset. Scale bar is equal to 100 nm.

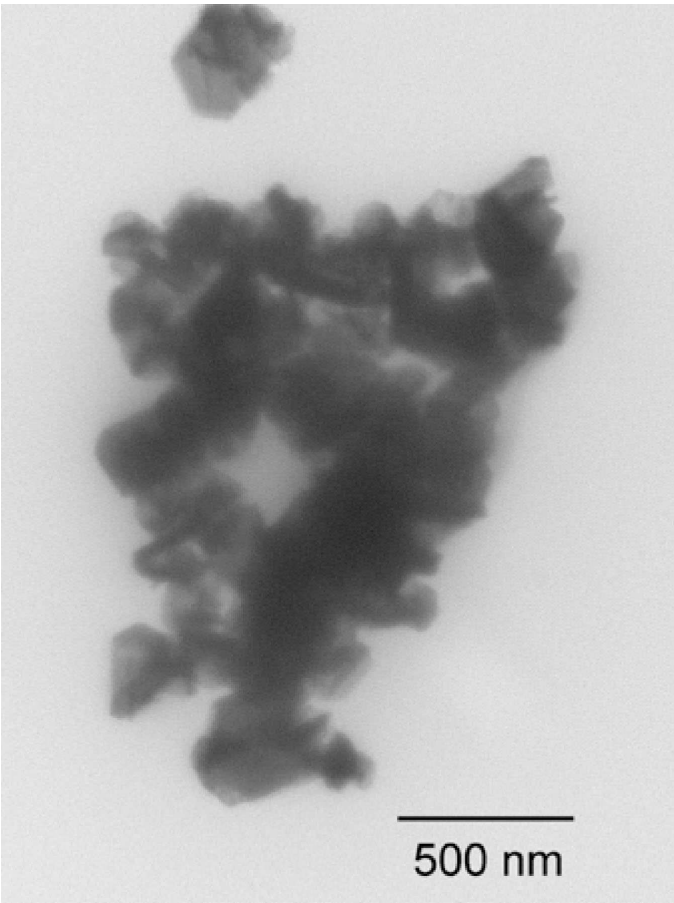

Figure 2.5: TEM image of Bi_2Te_3 synthesized in the absence of thiol.

Powder XRD patterns of the particles (Figure 2.6) exhibit peaks that correspond solely to the rhombohedral phase of Bi_2Te_3.[15] Broadening of the peaks in the diffraction patterns is much more pronounced in the smaller sized particles than the peak broadening of the patterns of larger particles, which is to be expected for nanostructured materials. Only peaks corresponding to bismuth and tellurium are present in EDS spectra (Figure 2.7) with a relative area matching the expected 2:3 stoichiometry.

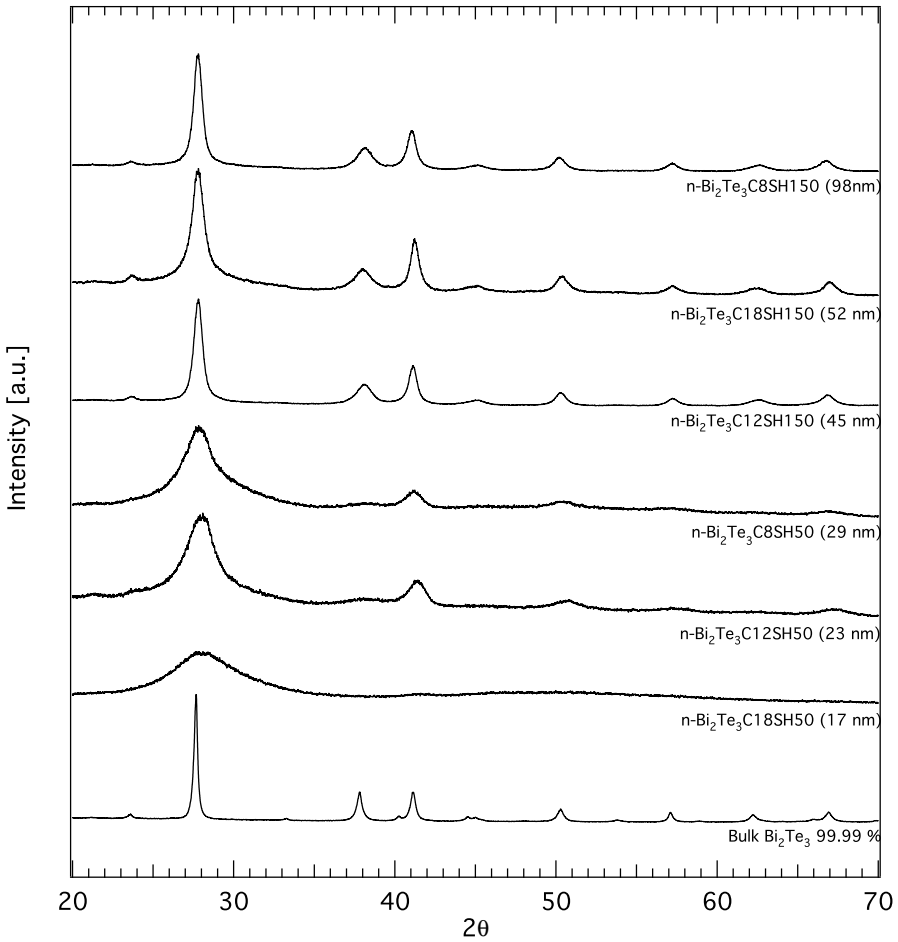

Figure 2.6: Powder X-ray diffraction of as-synthesized nanostructured bismuth telluride, n–Bi_2Te_3.

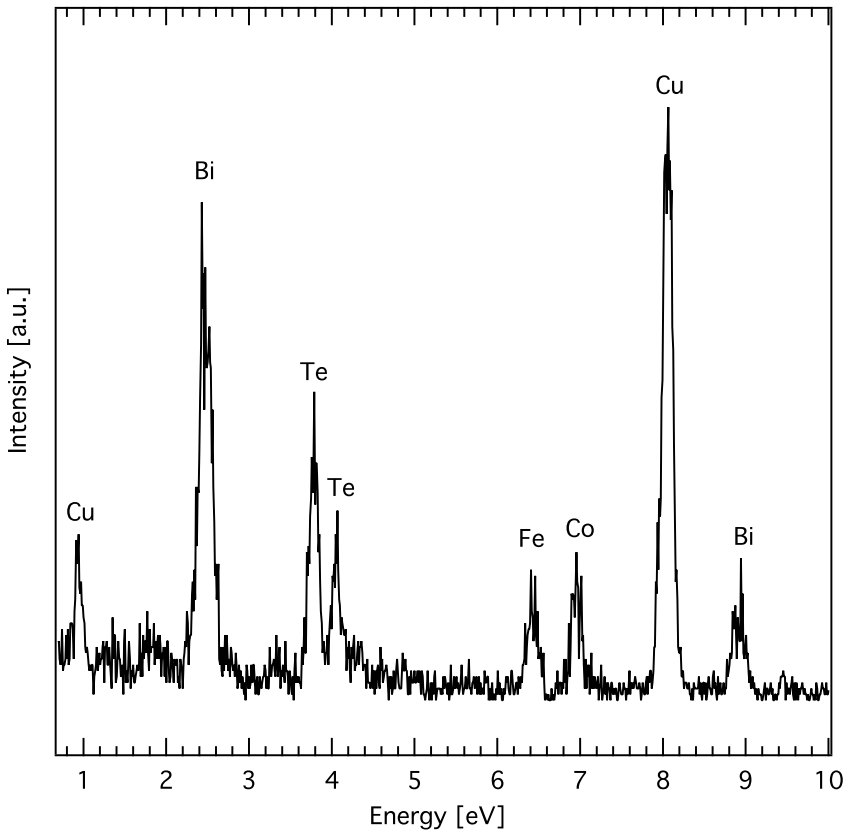

Figure 2.7: A representative EDS spectrum of nanostructured bismuth telluride (Cu peaks are due to the copper grid the sample is dispersed upon, Fe and Co peaks are artifacts from the electron gun).

The surface properties of the particles were investigated via NMR and XPS. The presence of the thiol capping ligand was confirmed from ^{1}H NMR spectra of solutions of the nanoparticles with resonances in the alkyl region that integrate correctly. XPS, which probes the material only to a depth of a few nanometers, also reveals core-level peaks for bismuth and tellurium that correspond to bismuth telluride (Figure 2.8). Small peaks due to carbon and oxygen are also observed due to the polymeric support upon which the sample was dispersed. A high-resolution scan of the Bi 4f region shows peaks at 162.4 and 157.2 eV, which correspond to the reported values for the binding energies of Bi $4f_{\frac{5}{2}}$ and Bi $4f_{\frac{7}{2}}$ of Bi_2Te_3, respectively. Additionally, a high resolution scan of the Te 3d region shows peaks at 582.4 and 572.2 eV, which match the reported values for the binding energies of Te $3d_{\frac{3}{2}}$ and Te $3d_{\frac{5}{2}}$ of Bi_2Te_3, respectively. Small peaks at 586.4 and 575.8 eV in the Te 3d region and small shoulders towards higher binding energy of the Bi 4f peaks correspond to $Bi_2Te_{3-x}O_x$.[16]

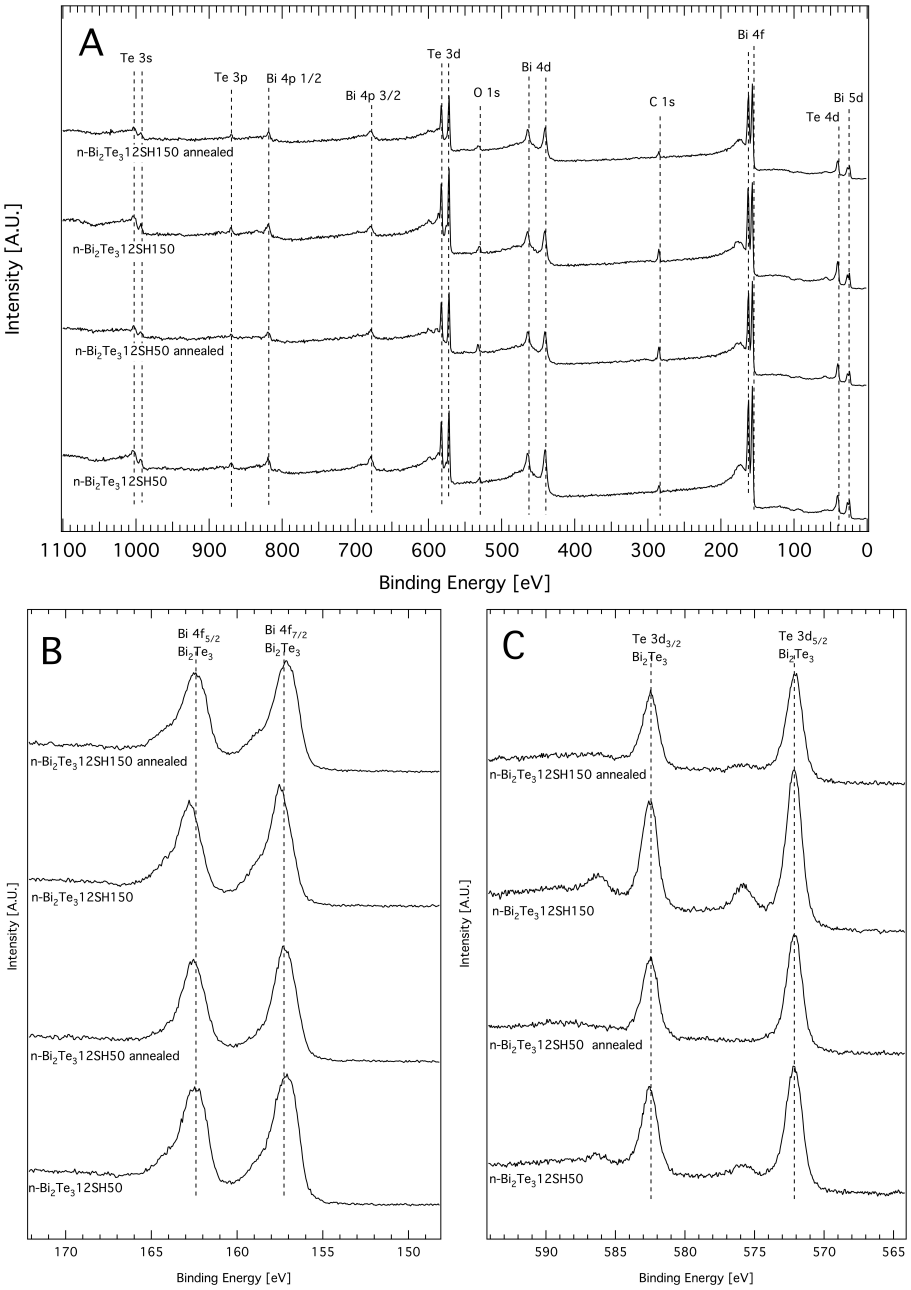

Figure 2.8: XPS data of annealed and unannealed n–Bi_2Te_3C12SH50 and n–Bi_2Te_3-C12SH150: A: survey scan, B: high resolution scan of the Bi 4f region, and C: high resolution scan of the Te 3d region.

The thermal properties of the bismuth telluride nanoparticles were investigated via TGA and DSC. TGA reveals that the thiol begins to desorb from the nanoparticles at ~275 °C while their melting temperature was determined to be ~420 °C (vs. 580 °C for the bulk) by DSC, providing a temperature window where thiols can be removed but the nanostructured architecture of the particles is retained (Figure 2.9). Powder XRD patterns collected after annealing at 350 °C under a constant flow of nitrogen for 24h exhibit sharpening of the Bragg peaks (Figure 2.10), suggesting some nanoparticle growth via sintering, and new peaks associated with the formation of a very small amount of oxide impurity. XPS spectra of annealed nanoparticles show a very small amount of oxide (Figure 2.8). However the material still remains almost entirely rhombohedral Bi_2Te_3. Field-emission scanning electron microscope (FESEM) images of annealed samples confirm that the nanoparticles have only slightly increased in size (Figure 2.11). Average particle size and size distribution of the as-synthesized nanoparticles was determined by analysis of 200 nanoparticles imaged in FESEM micrographs (Table 2.1). Thus it can be concluded that the nanoarchitecture of the particles is largely preserved after annealing.

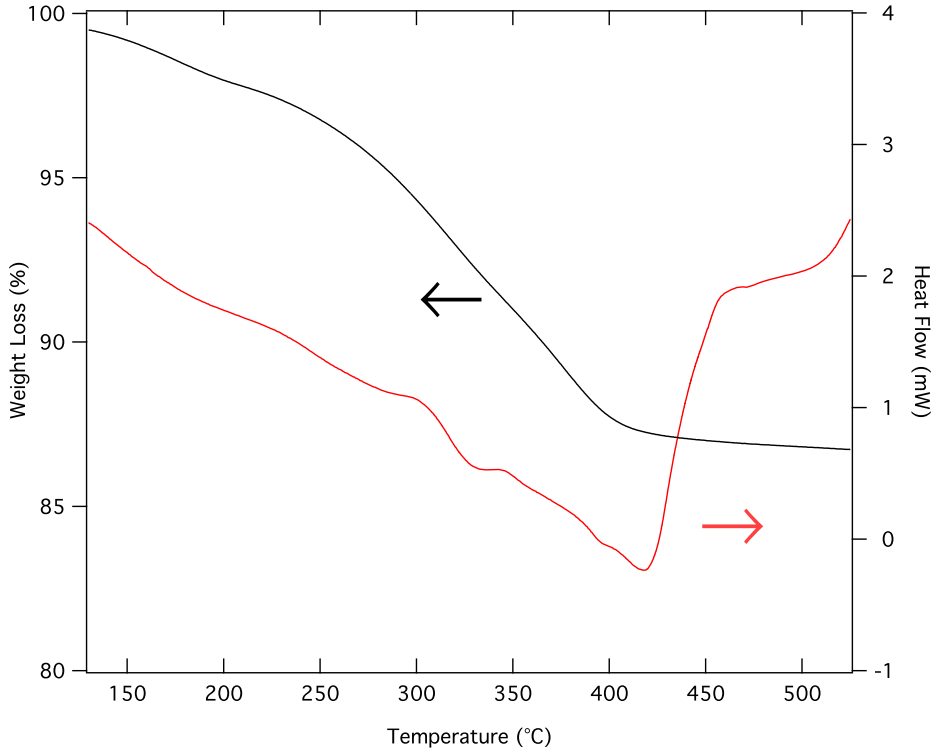

Figure 2.9: Representative DSC (exotherm up) and TGA plots of n–Bi_2Te_3C8SH50.

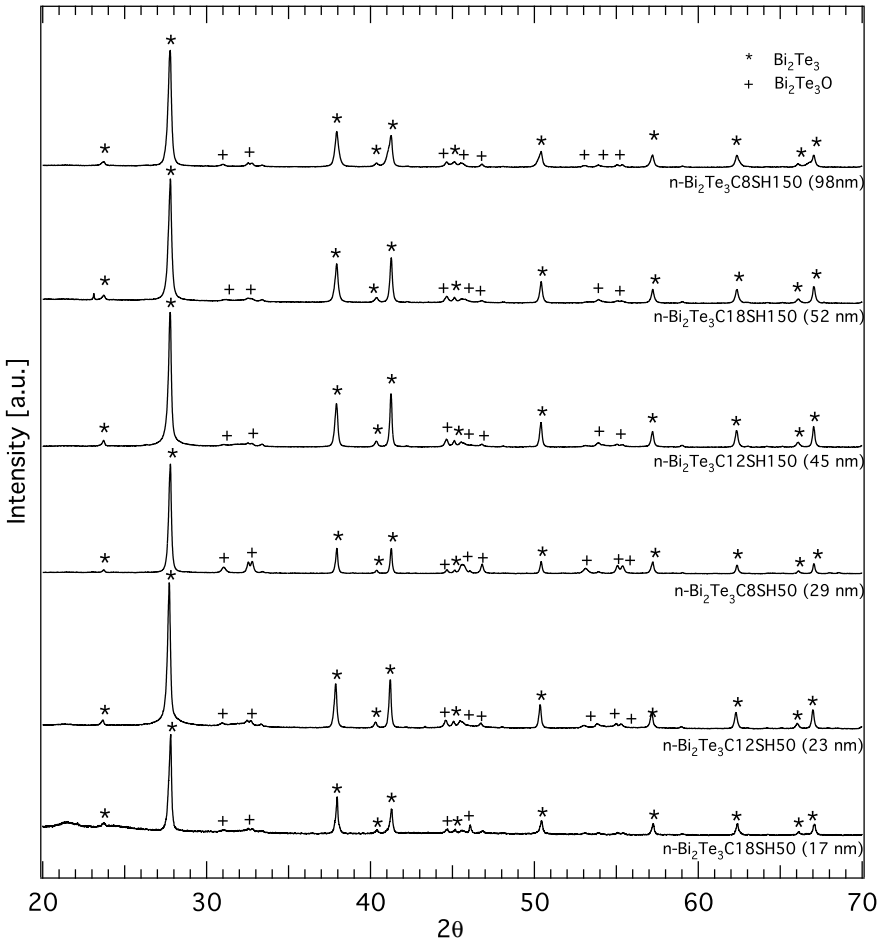

Figure 2.10: Powder X-ray diffraction of annealed nanostructured bismuth telluride, n–Bi_2Te_3.

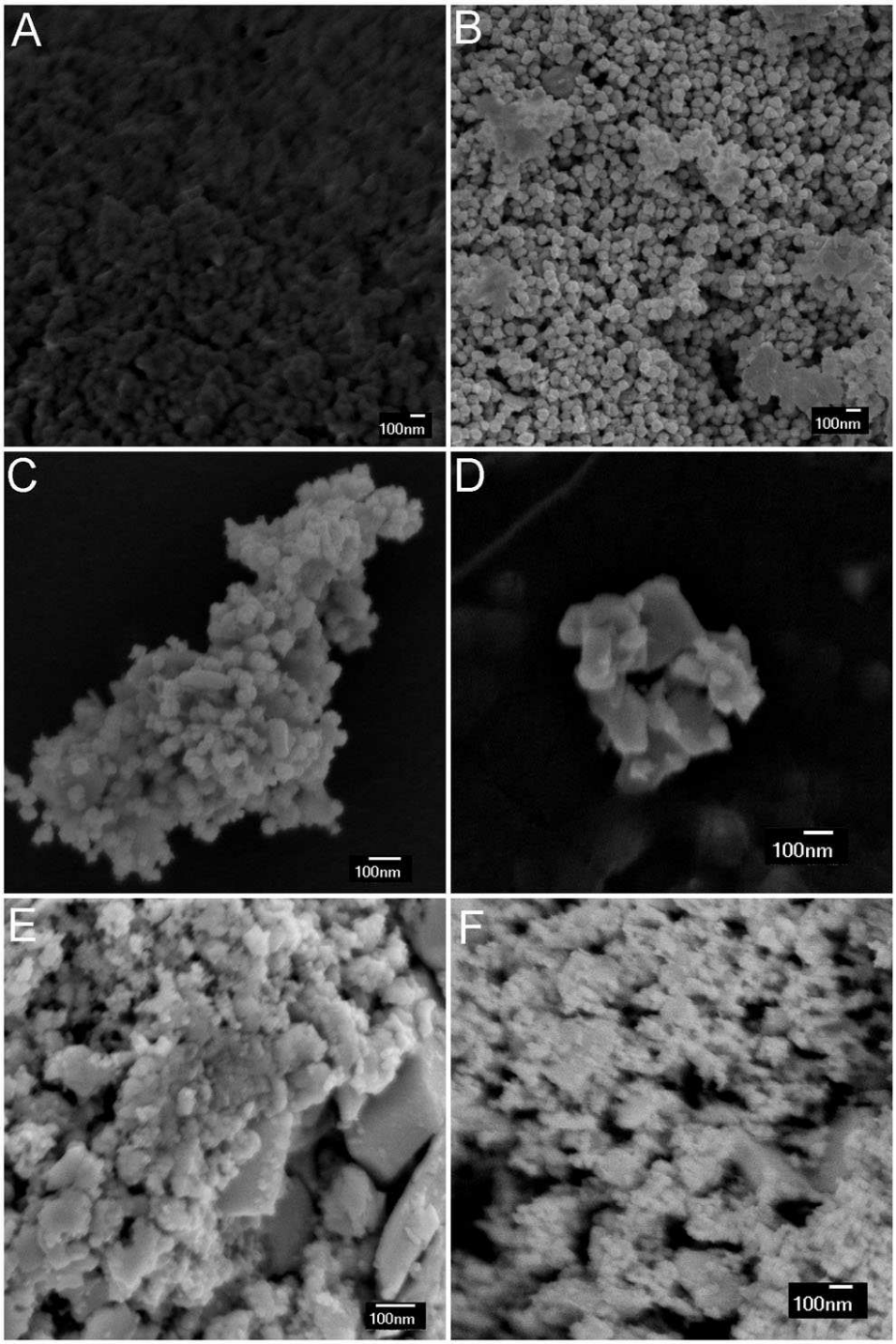

Figure 2.11: FESEM images of annealed nanostructured bismuth telluride particles: A: n–Bi_2Te_3C8SH50, B: n-Bi2Te3C8SH150, C: n-Bi2Te3C12SH50, D: n-Bi2Te3-C12SH150, E: n-Bi2Te3C18SH50, F: n-Bi2Te3C18SH150.

2.4 Thermoelectric Properties of Nanostructured Bismuth Telluride

The thermoelectric transport properties of unannealed bismuth telluride nanoparticles (Table 2.1) are poor due to the presence of the insulating capping agent. In some case the electrical conductivity for unannealed bismuth telluride nanoparticles was six orders of magnitude lower than a pellet of pure bulk bismuth telluride prepared in the same manner. Low electrical conductivity of these materials could be expected given that each particle is coated with an insulating layer of thiol. This would greatly decrease the amount of interparticle communication leading to a highly resistive sample. Using the thermal analysis as a guideline, it was found that there is a temperature range over which the thiols may be removed but the nanoparticles retain their morphology.

As observed through DSC and TGA; there exists a window of temperatures between ~275 °C and ~420 °C where the thiols desorb from the nanoparticle surface but the nanostructured nature of the material remains intact. Annealing creates much closer interparticle distances, thereby increasing the electrical conductivity of the samples. (Figure 2.12). The nanoparticles were annealed at 350 °C under a constant flow of nitrogen to minimize oxidation of the nanoparticle surface. After pressing these particles into pellets for properties measurements, densities as high as 87% of the bulk density of bismuth telluride were realized, as determined by mass and volume measurements. FESEM images of cross-sections of compressed pellets show very small grain boundaries, again confirming that the nanostructured nature of the materials is retained after annealing. After annealing and pressing into pellets, the largest improvements in thermoelectric power and electrical conductivity were observed for the smaller (< 40 nm) nanoparticles, which

increased in power factor (σS^2) by five or six orders of magnitude (Table 2.2). The largest thermoelectric powers are $-150\,\mu V\,K^{-1}$ and $-191\,\mu V\,K^{-1}$ for the samples with annealed particles sizes of $\sim 39\,nm$ and $\sim 34\,nm$ respectively, considerably larger than the value of $-107\,\mu V\,K^{-1}$ previously reported.[1] Electrical conductivity of ensembles of nanoparticles also increased to be approximately equal to that of a bulk bismuth telluride sample densified in the same manner. The materials are slightly n-doped, presumably due to sulfur from the capping agent.[17] Importantly, the current-voltage (I-V) behavior for all the samples is ohmic, in contrast to the non-ohmic behavior previously reported for a bismuth telluride sulfide phase, suggesting that impurities between the bismuth telluride grains are less prevalent and in agreement with the X-ray diffraction results that indicate much less impurity.

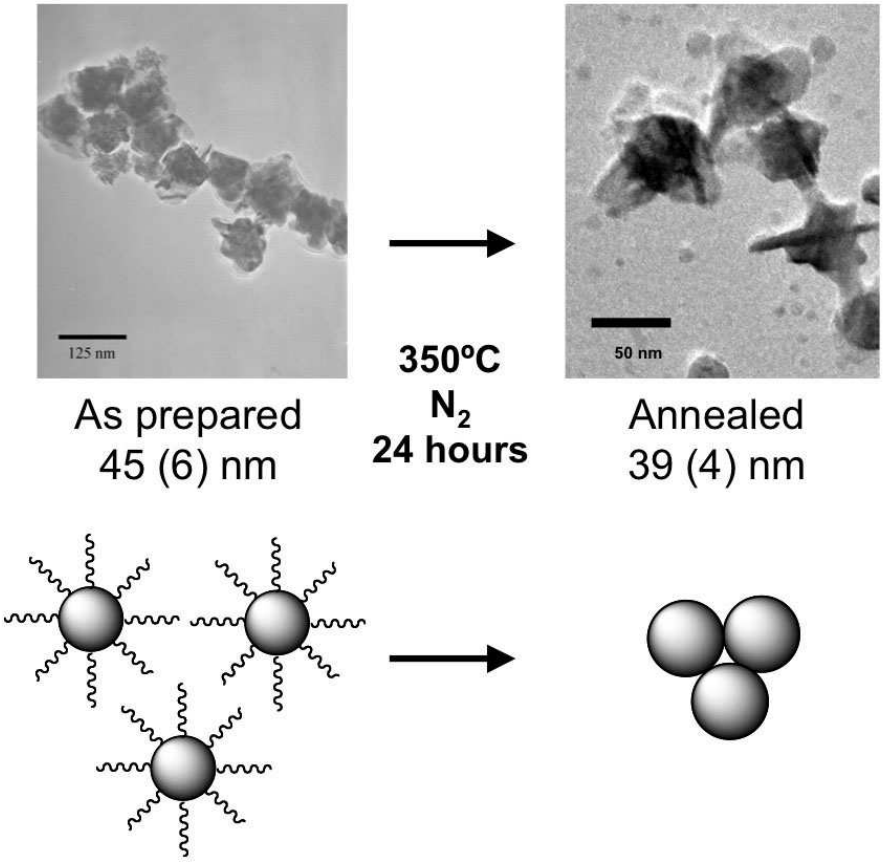

Figure 2.12: TEM micrographs of as-prepared and annealed n–Bi_2Te_3C12SH150 and a schematic representation of the annealing process.

The carrier concentration of the annealed 39 nm particles determined via Hall Effect measurements was $1.50(9) \times 10^{21}\,\mathrm{cm}^{-3}$, higher than the carrier concentrations of the 86 nm particles ($9.2(1) \times 10^{19}\,\mathrm{cm}^{-3}$) or that of optimized commercial antimony bismuth telluride ($\sim 3.0 \times 10^{20}\,\mathrm{cm}^{-3}$). The higher carrier concentration in the smaller sized particles is likely a result of increased sulfur doping from the thiol ligands. Smaller size particles have a higher surface area to volume ratio and, thus, proportionately more capping agent. It will be necessary to have more uniformly doped samples to interpret size effects on the transport properties, which may be significant for the smallest particles synthesized in this work. However, the sulfur content is still sufficiently low to prevent the formation of a new sulfide phase upon annealing, in contrast to previous reports of the formation of a material that is primarily bismuth telluride sulfide after a heating step to drive off the capping agent.

The steady-state thermal conductivity of annealed octanethiol-capped bismuth telluride nanoparticles synthesized at 50 °C (60 nm) was measured from 300 to 30 K in a radiation-shielded vacuum probe in a custom-designed closed-cycle refrigerator with a maximum uncertainty of 8% at 300 K. At best, the thermal conductivity shows a very weak dependence on temperature (Figure 2.13). This absence of temperature dependence is atypical of crystalline solids and is an indication that phonon scattering other than from anharmonic interactions is present in this material. This is different than that observed in bulk crystalline Bi_2Te_3 and indicates that the nanoscale morphology of the sample has a significant effect on phonon transport. The thermal conductivity at room temperature is $0.51\,\mathrm{W\,m^{-1}\,K^{-1}}$. The mean phonon free path (l) estimated at room temperature using the relation, $\kappa_\mathrm{L} = \frac{1}{3} C_\mathrm{v} v l$, where κ_L is the measured thermal conductivity ($0.51\,\mathrm{W\,m^{-1}\,K^{-1}}$), C_v is the heat capacity ($1.2 \times 10^6\,\mathrm{J\,K^{-1}\,m^{-3}}$),[18] and v is the speed of sound ($2.35 \times 10^3\,\mathrm{m\,s^{-1}}$),[19]

is 5 Å at room temperature. This is smaller than our average grain size but suggests substantial scattering due to the nanoscale morphology. For comparison, the minimum thermal conductivity for Bi_2Te_3 calculated using Cahill's model, a lower bound,[20] is $0.12\,W\,m^{-1}\,K^{-1}$. Single crystal bulk Bi_2Te_3 has a room temperature thermal conductivity of $\sim 2.0\,W\,m^{-1}\,K^{-1}$.[21]

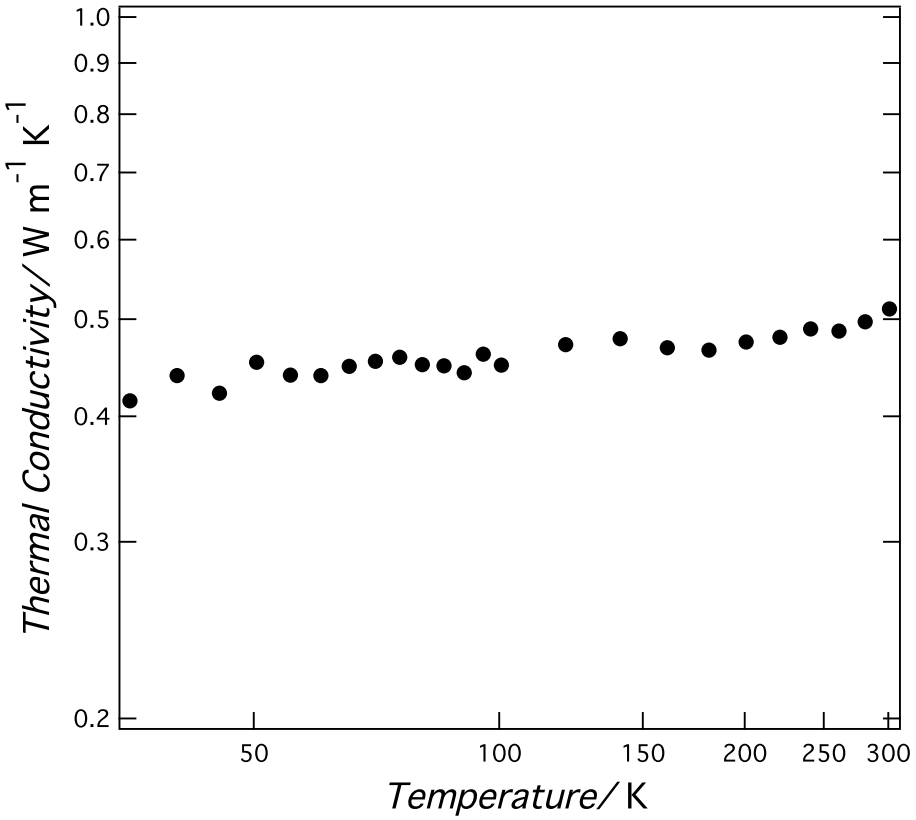

Figure 2.13: Temperature dependence of the thermal conductivity of annealed n–Bi_2Te_3C8SH50 (annealed particle size, 60 nm).

2.5 Conclusions

The synthesis of size-tuned nanostructured, thiol-capped bismuth telluride with relatively low size dispersity has been successfully completed. Reaction temperature and length of the alkane thiol used to cap the bismuth telluride nanostructures allowed a certain amount of control over the resulting crystalline nanostructures. Higher temperatures and longer alkyl chain length of the capping ligand resulted in smaller nanoparticles. Transport properties of these structures were promising, however they could be improved through proper doping and improved interparticle transport.

Optimizing ZT of thermoelectric materials requires maximizing the thermoelectric power and electrical conductivity while minimizing the thermal conductivity. The interdependencies between these quantities are what makes optimizing ZT in general so challenging. The results reported here represent a significant step towards improving the materials quality of chemically synthesized bismuth telluride nanoparticles to allow for measurement and ultimately optimization of these three quantities, two of which (electrical and thermal conductivities) have not been previously reported for similar materials, likely due to issues with materials purity and density. The thermal conductivity of the annealed 60 nm Bi_2Te_3 particles is ~ 2 times lower than that of the best ball-milled p-type nanostructured antimony bismuth telluride while the thermoelectric power is only somewhat less.[2] Thus the largest improvement in ZT will come from improving the electrical conductivity, which can be accomplished by further reducing the impurity content of the annealed and pressed materials and through appropriate doping. Given the purity of the annealed and pressed materials, doping studies are the next logical step to optimizing the electrical conductivity. We have synthesized

high purity size-controlled Bi_2Te_3 nanoparticles and have improved the density of the material enough to allow for the thermal conductivity measurements, but further reductions in porosity will likely also improve the electrical transport. If the electrical conductivity can be improved while the thermoelectric power and thermal conductivity are maintained at least at their present values, ZT in excess of the state-of-the-art will become possible.

2.6 Experimental

All chemicals were degassed and all manipulations were carried out under an N_2 atmosphere. Bismuth neodecanoate (technical grade), octanethiol (98.5%), dodecanethiol (98+%), octadecanethiol (98%), and phenyl ether (99%) were obtained from Sigma-Aldrich. Tellurium powder (99.99%) was obtained from Alfa Aesar. Trioctylphosphine (97%) was obtained from Strem Chemicals.

In a typical synthesis, bismuth neodecanoate (1.0 mmol) was injected into preheated (either 50 °C or 150 °C) diphenyl ether (50 mL) in a 250 mL flask under N_2. To this, the thiol capping ligand (50 mmol) was injected. The reaction mixture turned black upon the addition of Te (1.5 mmol), 0.5 M Te in trioctylphosphine, prepared by stirring tellurium in trioctylphosphine) to the solution. Thiol-capped Bi_2Te_3 was separated by centrifugation and washed with toluene. The resulting black powder was dried under high vacuum and used for further characterization.

Powder XRD patterns were taken with a Rigaku (RU-200) high-brilliance X-ray generator equipped with a Guinier camera (G670 from Huber Diffraktiontechnik GmbH & Co. KG) using monochromatized Cu Kα (λ = 1.5418 Å) radiation. TEM micrographs were recorded on a JEOL 2010 LaB6 instrument operating at 200 kV. FESEM micrographs were recorded on a JEOL 6700F operating at 3 kV. NMR spectra were collected using a Bruker CDPX 300 MHz spectrometer. Powders were densified using a Carver lab press and pellet die, resulting in pellets that measured 0.125 mm in radius and between 7 mm and 2 mm in length. Thermoelectric power measurements were made using a reported in-house instrument.[22] Electrical conductivity was calculated by measuring the sample dimension and sample resistance using the four-probe technique. Carrier concentrations were determined through Hall effect measurements on 6 × 6 mm squares of pressed, annealed

nanostructured bismuth telluride of thicknesses between 0.3 and 0.5 mm. The Hall voltage was determined at +2.0 T, no field, and −2.0 T using an electromagnet and Stanford Research System lock-in amplifiers (SR830). Thermal studies were conducted using a DSC (TA Instruments 2420) and TGA (TA instruments Q600) at a heating rate of 10 °C per minute under nitrogen. UV-Vis spectra were taken using a Hewlett-Packard 8453 diode-array UV-visible spectrometer. X-ray photoelectron spectra of bismuth telluride nanoparticles were acquired using a Surface Science Instruments model SSX-100 instrument with Al Kα probe beam.

2.7 References

[1] Purkayastha, A.; Kim, S.; Gandhi, D.; Ganesan, P.; Borca-Tasciuc, T.; Ramanath, G. *Adv. Mater.* **2006**, *18*, 2958–2963.

[2] Poudel, B.; Hao, Q.; Ma, Y.; Lan, Y.; Minnich, A.; Yu, B.; Yan, X.; Wang, D.; Muto, A.; Vashaee, D.; Chen, X.; Liu, J.; Dresselhaus, M.; Chen, G.; Ren, Z. *Science* **2008**, *320*, 634–638.

[3] Sander, M.; Gronsky, R.; Sands, T.; Stacy, A. *Chem. Mater.* **2003**, *15*, 335–339.

[4] Sapp, S.; Lakshmi, B.; Martin, C. *Adv. Mater.* **1999**, *11*, 402–404.

[5] Deng, Y.; Nan, C.-W.; Wei, G.-D.; Guo, L.; Lin, U. *Chem. Phys. Lett.* **2003**, *374*, 410–415.

[6] Zhao, X.; Ji, X.; Zhang, Y.; Cao, G.; Tu, J. *App. Phys. A.* **2005**, *80*, 1567–1571.

[7] Foos, E.; Stroud, R.; Berry, A. *Nano. Lett.* **2001**, *1*, 693–695.

[8] Watanabe, N.; Kawamata, J.; Toshima, N. *Chem. Lett.* **2004**, *33*, 1368–1369.

[9] Lu, W.; Ding, Y.; Chen, Y.; Wang, Z.; Fang, J. *J. Am. Chem. Soc.* **2005**, *127*, 10112–10226.

[10] Purkayastha, A.; Lupo, F.; Kim, S.; Borca-Tasciuc, T.; Ramanath, G. *Adv. Mater.* **2006**, *18*, 496–500.

[11] Reddy, V.; P. Garrity, P.; Stokes, K. *Mat. Res. Soc. Symp. Proc.* **2004**, *793*, S8.36.1–S8.36.5.

[12] Ni, H.; Zhao, X.; Zhu, T.; Ji, X.; Tu, J. *J. Alloys Compd.* **2005**, *397*, 317–321.

[13] Toprak, M.; Zhang, Y.; Muhammed, M. *Mater. Lett.* **2003**, *57*, 3976–3982.

[14] Reader, J.; Corliss, C. *CRC Handbook of Chemistry and Physics*, 87th ed.; CRC Press, 2006.

[15] McClune, W. *Powder Diffraction File*; JCPDS International Center for Diffraction Data; pp Index Card No. 15–863.

[16] Bando, H.; Koizumi, K.; Oikawa, Y.; Daikohara, K.; Kulbachinskii, V.; Ozaki, H. *J. Phys. Condens. Mat.* **2000**, *12*, 5607–5616.

[17] Durst, T.; Goldsmid, H. J.; Harris, L. B. *Solar Energy Mater.* **1981**, *5*, 181–186.

[18] Hicks, L.; Dresselhaus, M. *Phys. Rev. B.* **1993**, *47*, 16631–16634.

[19] Hellewege, K.; Madelung, O. *Numerical Data and Functional Relationships in Science and Technology*; Springer-Verlag; Vol. 17, p 275.

[20] Cahill, D.; Watson, S.; Pohl, R. *Phys. Rev. B.* **1992**, *46*, 6131–6140.

[21] Scherrer, H.; Scherrer, S. *Thermoelectrics Handbook Macro to Nano*; Taylor and Francis, 2006; Vol. 2, p 16 ch. 27.

[22] Polvani, D.; Meng, J.; Hasegawa, M.; Badding, J. *Rev. Sci. Instr.* **1999**, *70*, 3586–3589.

Chapter Three

Fabrication of Antimony Telluride Nanowires and Thin Films via Simple Solution Methods

3.1 Introduction

Antimony telluride is a compound of interest in the fields of thermoelectrics and nonvolatile memory. Nanostructuring this material could led to improved materials properties and ease of integration into devices. There have been few reports of nanostructured antimony telluride in the literature. Solvothermal methods have lead to antimony telluride nanoplatelets, anisotropic nanostructures, and nanowires.[1,2] Without the addition of a surfactant or template, thin platelets are formed due to the anisotropic layered nature of the crystal structure of antimony telluride. Antimony telluride nanowires have also been fabricated by vapor-liquid-solid growth (VLS) and electrodeposition in porous alumina membranes.[3–5] Antimony telluride thin films have been fabricated by vacuum and electrochemical deposition.[6,7]

Nanowires of various materials, be they organic, polymeric, or inorganic, have received much attention since the 1990s.[8] The pioneering work of Martin and coworkers using nanoporous membranes as hard templates for the synthesis of nanowires has led to a rich field of scientific discovery.[9] Templated synthesis of nanostructures within nanoporous membranes is a cost effective, high-throughput and relatively simple alternative to high vacuum methods like vapor-liquid-solid (VLS) growth. Low-cost, high-throughput processing of these materials would be highly desirable.

Mitzi et al. have shown how versatile the reducing solvent hydrazine can be for the dissolution of many semiconducting chalcogenides.[10] Thin films of $SnSe_2$ and SnS_2,[11] ZnTe,[12] and In_2Te_3[13] and In_2Se_3,[14] for thin film transistor (TFT) devices and CIGS (Cu-In-Ga-Se/S)[15] thin films for photovoltaic applications have been fabricated by this method. Briefly, thin films are prepared by the dissolu-

tion of elements or compounds in hydrazine, spincoating, and subsequent thermal treatment of the precursor to yield the semiconductor of interest. The dissolution of antimony telluride in hydrazine has not been reported in the literature. In this chapter, a method is described which takes advantage of the solvating properties of hydrazine and combines it with the simplicity of templated nanowire synthesis to produce antimony telluride nanowires and antimony telluride/tellurium nanowire composites. This templating method provides a simple, cost-effective, and high-throughput method for the fabrication of semiconductor nanowires. Furthermore, the diameter of the nanowires can be selected by using alumina templates of varying pore size. Antimony telluride thin films are also fabricated by simple evaporation. Electronic property measurements on these films show promising electrical conductivity and thermoelectric power.

3.2 Synthesis and Properties of a Soluble Antimony Telluride Precursor

The soluble antimony precursor is prepared by adding appropriate amounts of antimony telluride and tellurium to the solvent hydrazine. It is known that the solubility of the metal chalcogenide in hydrazine is greatly improved when an amount of elemental chalcogenide is added to the solution.[16] To explore the effect of the amount of elemental tellurium has on the solubility of antimony telluride in hydrazine, precursor solutions were prepared using varying antimony telluride/tellurium ratios (Table 3.1).

Table 3.1: Conditions for the synthesis of precursor solutions used in the fabrication of antimony telluride nanowires and thin films.

Solution ID[a]	Sb_2Te_3 (mmol)	Te (mmol)	Sb_2Te_3:Te	N_2H_4 (mL)
A	0.225	0	1:0	3
B	0.225	0.0225	10:1	3
C	0.225	0.0450	5:1	3
D	0.225	0.113	2:1	3
E	0.225	0.225	1:1	3

[a] All solutions stirred under an inert N_2 atmosphere for 10 days

Hydrazine serves multiple purposes in the preparation of the precursor and in the formation of the final material: First, it serves as a reducing agent converting the neutral antimony telluride into anionic species. Secondly, nascent hydrazinium ions serve to solvate the anionic species and prevent preciptation. Thirdly, upon annealing the byproducts of any residual hydrazine will decompose to N_2 and H_2.[17] The antimony telluride/tellurium solutions take on a deep red-orange color. Presumably, the red precursor solutions are anionic species stabilized by hydrazinium cations. The dissolution of antimony telluride is proposed to occur through the reaction:

$$10\,N_2H_4 + 5\,Te + Sb_2Te_3 \longrightarrow 2\,N_2 + 8\,N_2H_5^+ + 2\,SbTe_3^{3-} + Te_2^{2-}$$

This proposed reaction is supported by the evolution of gas as the reaction progresses. The true chemical identity of the anionic species is unknown; attempts to crystallize any of the precursor solutions by slow diffusion of nonsolvents, such as toluene, results in precipitation of an amorphous powder.

The thermal properties of the precursors were investigated via DSC and TGA. Solid powders of the precursor were obtained by drop-casting the hydrazine solutions onto glass slides and allowing the hydrazine to evaporate in an inert atmosphere at room temperature. TGA data is presented in Figures 3.1 and 3-2. All precursors, regardless of tellurium content, display a ~2% weight loss at ~150 °C; this corresponds to a loss of residual hydrazine in the precursor. A second weight loss from 250–350 °C is due to excess chalcogen (Figure 3.1).[18] The TGA shows little weight loss between 350–500 °C (Figure 3.2). At temperatures above 500 °C the precursors show similar weight loss to that of bulk antimony telluride, which corresponds to the vaporization of tellurium due to its relatively higher vapor pressure compared to antimony.[19] DSC plots of the precursor solution (Figure 3.3) match closely to that of bulk antimony telluride showing a melt transition at 412 °C, corresponding to the presence of both antimony telluride and tellurium.[20]

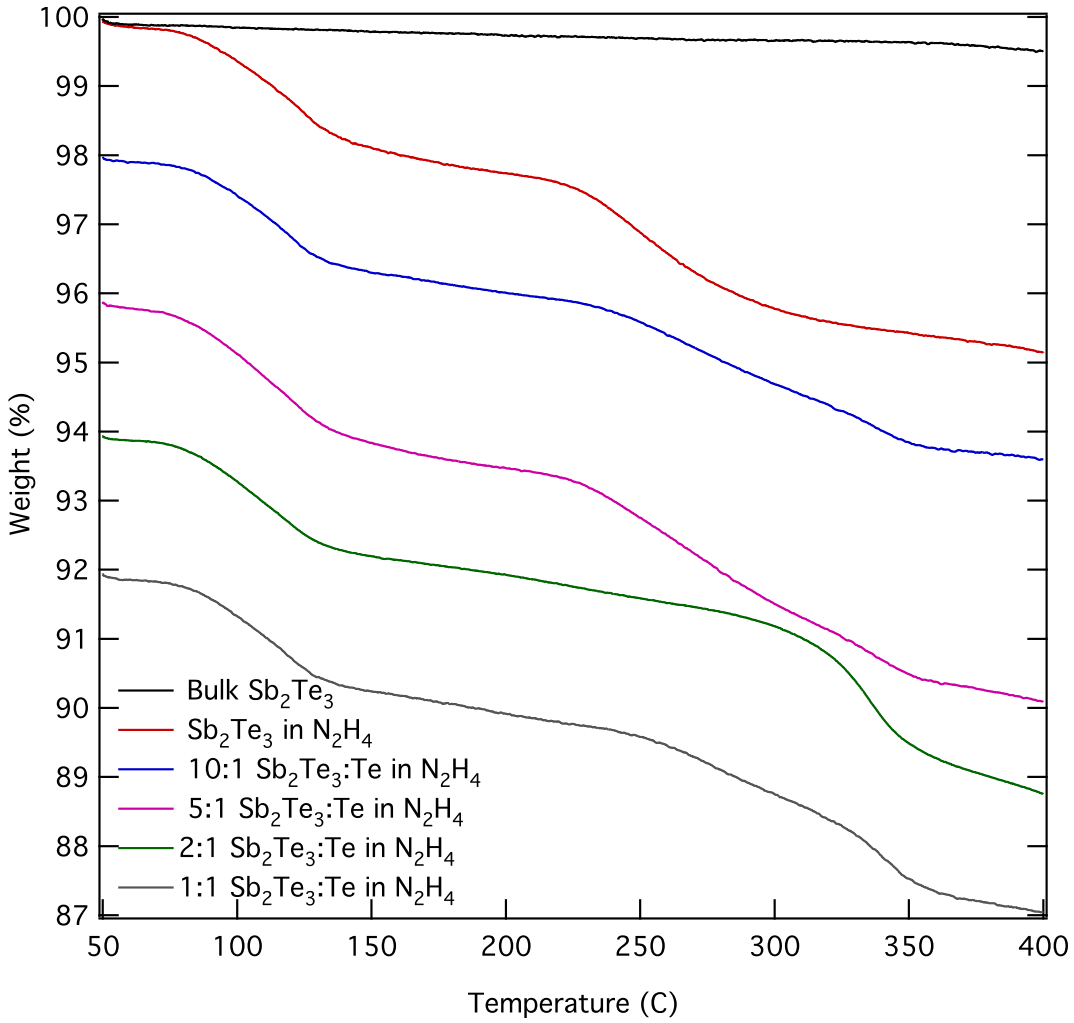

Figure 3.1: Low temperature range TGA data of antimony telluride precursors of varying tellurium content compared with bulk antimony telluride.

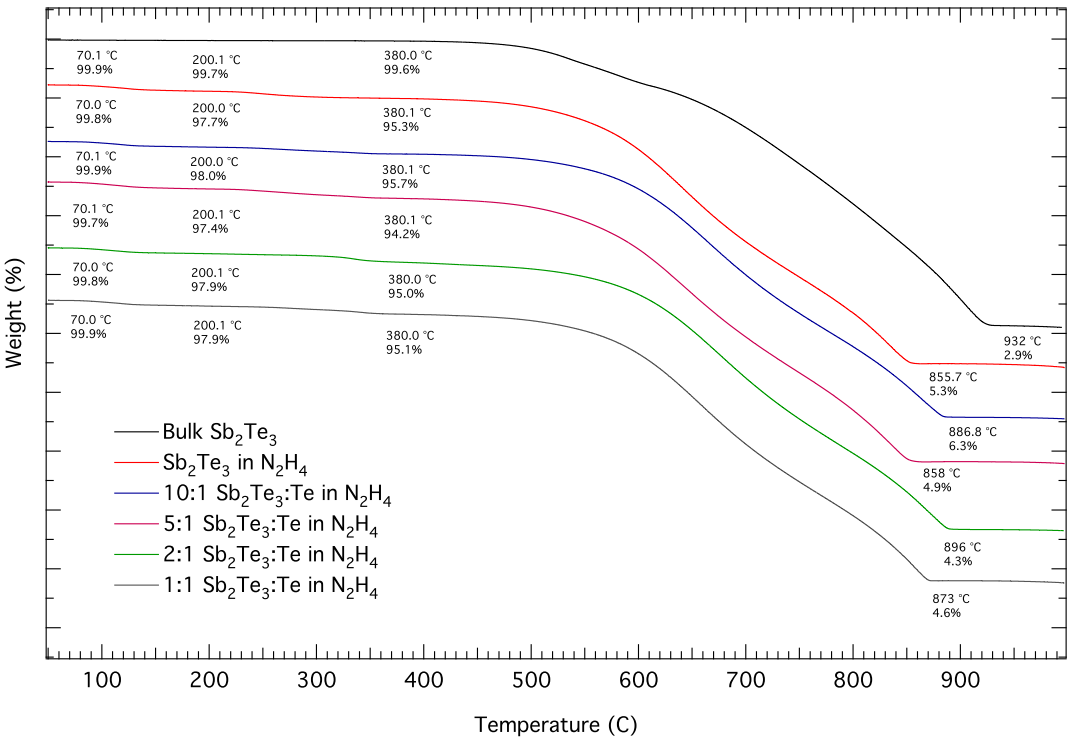

Figure 3.2: TGA data of antimony telluride precursors of varying tellurium content compared with bulk antimony telluride.

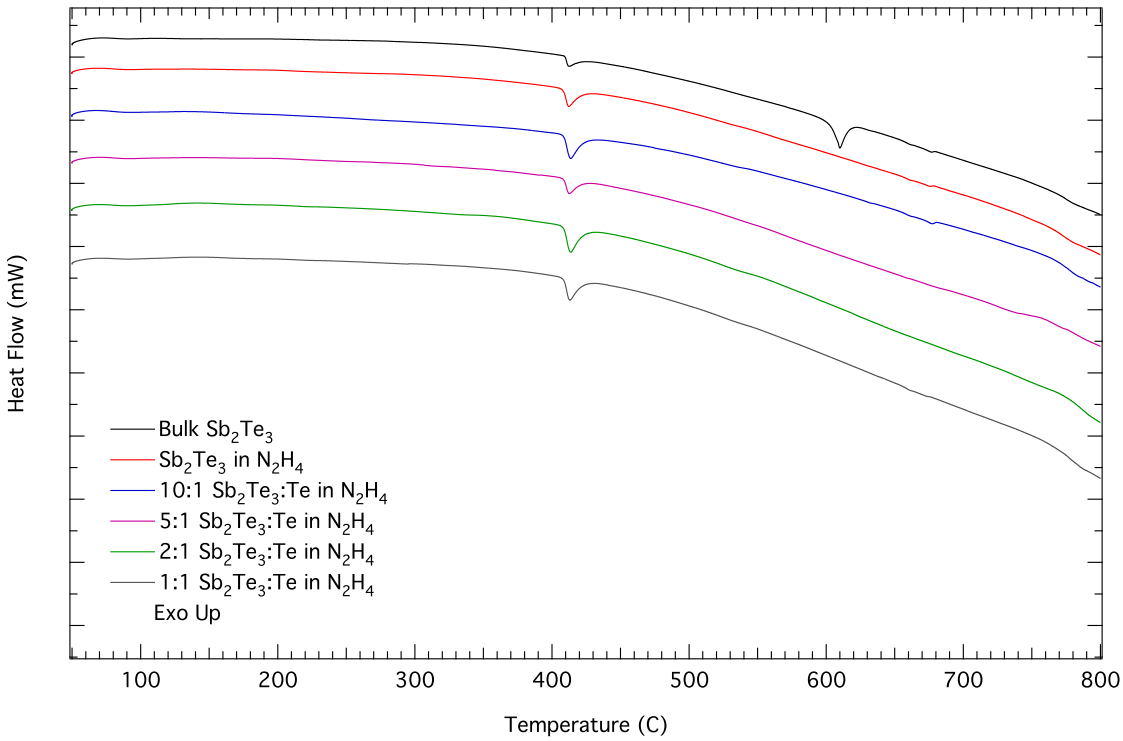

Figure 3.3: DSC data of antimony telluride precursors of varying tellurium content compared with bulk antimony telluride.

3.3 Antimony Telluride Nanowires via Simple Templating Method

Antimony telluride nanowires were fabricated by simple solution deposition of the precursor in alumina templates. Annealing of the membranes containing precursor solutions completes nanowire formation. The membrane can be chemically etched leaving a solution of bare nanowires.

The morphology of the nanowires has been investigated by FESEM. Figure 3.4 shows FESEM images of the fabricated nanowires from each of the antimony telluride/tellurium precursor solutions. The nanowires appear to have a rough outer surface composed of many crystallites. This rough surface could be advantageous for the application of these materials as thermoelectrics. Reducing the thermal conductivity of a material without sacrificing electrical conductivity is a major hurdle in designing high performance thermoelectrics. The smaller crystallites could provide a way to scatter phonons, thus reducing the thermal conductivity while the close proximity of the crystallites comprising the nanowire could allow for electrical conductivity. This has been shown to be true for other thermoelectric materials.[21] The nanowires have a diameter of ~250 nm, which approximately matches the diameter of the pores of the alumina templates (~200–~300 nm). Some larger and smaller nanowires are observed due to the branching of the commercially prepared alumina templates. To prove the versatility of this method, 100 nm nanowires were fabricated using alumina templates with a pore size of 100 nm (Figure 3.5). It has been observed that as the amount of tellurium added increases, the relative amount of wires being formed also increases which further confirms the increased solubility of antimony telluride with added tellurium. The solubility of antimony telluride in hydrazine is very low and no nanowires were observed when no tellurium was added to enhance the solubility

of antimony telluride (solution A, Table 3.1).

Wires were fabricated in an alumina membrane which had a thin (~100 nm) film of nickel evaporated onto the backside. Once the membrane was dissolved, the wires remain attached to the nickel segment creating a vertical array of nanowires. FESEM images of these wire arrays confirm that they are not tubular in nature but rather solid wires (Figure 3.6).

The composition of the nanowires was investigated via powder XRD and EDS. EDS spectra of the nanowires show peaks for both antimony and tellurium (Figure 3.7). The phase of the annealed material has been investigated by powder XRD of the nanowire arrays before being released from the alumina membranes (Figure 3.8). After annealing antimony telluride/hydrazine solutions (solution A, Table 3.1) pure rhombohedral antimony telluride is obtained; however, due to the low solubility of antimony telluride in hydrazine, no nanowires were observed. In antimony telluride/tellurium solutions where the antimony telluride:tellurium molar ratio is greater than 1 (solutions B–D, Table 3.1), pure rhombohedral antimony telluride nanowires are produced. The precursor in which there is an equimolar amount of antimony telluride and tellurium (solution E, Table 3.1) produces nanowires that are a composite of antimony telluride and elemental tellurium. Doping in bismuth and antimony telluride can be obtained by deviations from stoichiometry; an excess of tellurium will lead to n-doped material.[22] The added tellurium in the case of these nanowires would also act as an n-type dopant. It is interesting to note that the peak intensities match that of a random powder of antimony telluride, which further confirms that the nanowires are made of randomly oriented crystallites.

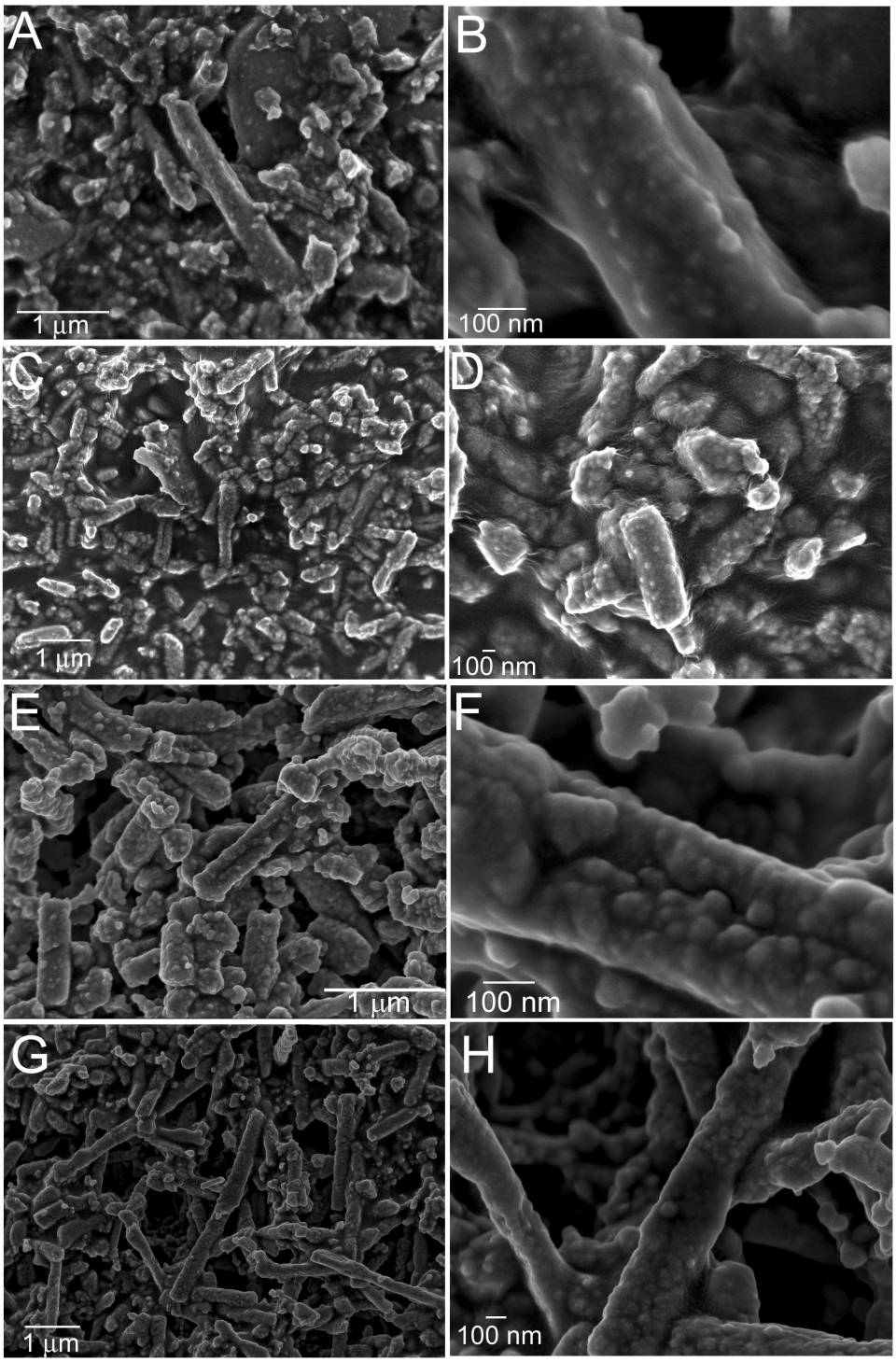

Figure 3.4: FESEM images of antimony telluride nanowires prepared by templating method: Low (A) and high (B) magnification images of nanowires obtained from solution B. Low (C) and high (D) magnification images of nanowires obtained from solution C. Low (E) and high (F) magnification images of nanowires obtained from solution D. Low (G) and high (H) magnification images of nanowires obtained from solution E.

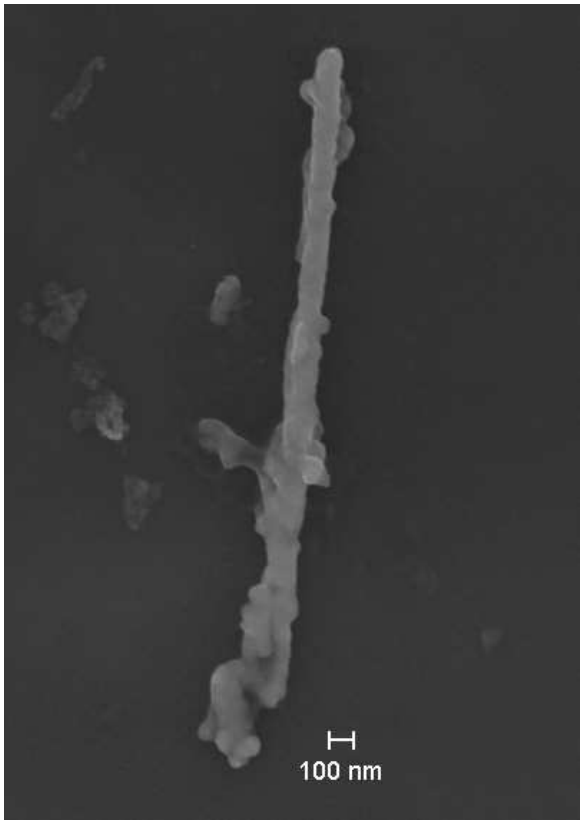

Figure 3.5: Antimony telluride nanowire of 100 nm diameter obtained from solution B.

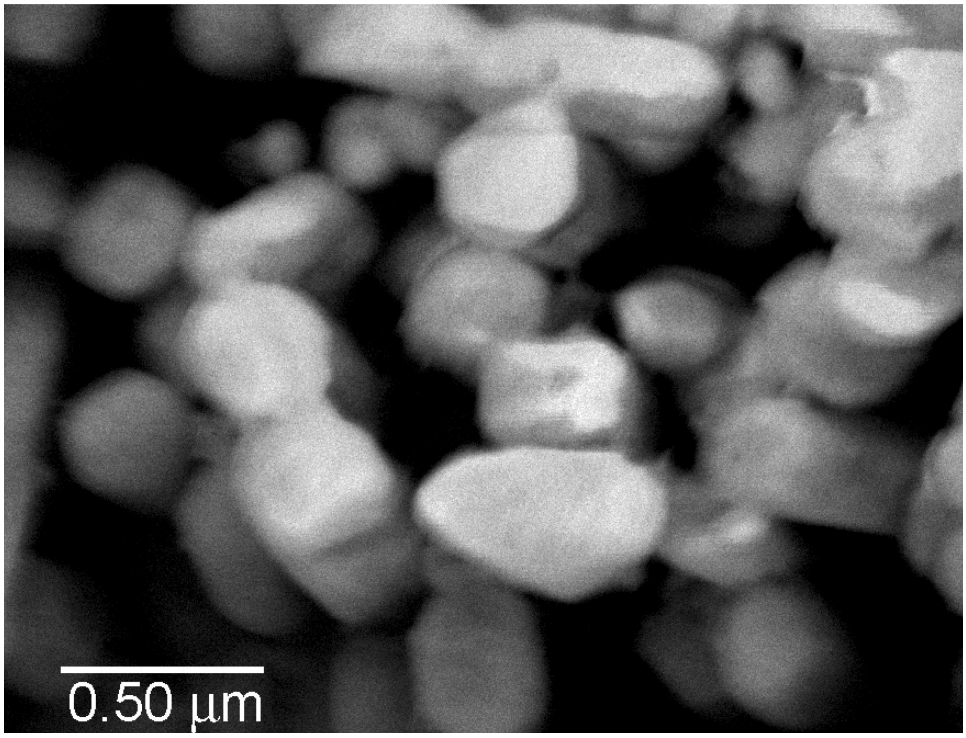

Figure 3.6: FESEM image of an axial view of antimony telluride nanowires obtained from solution B.

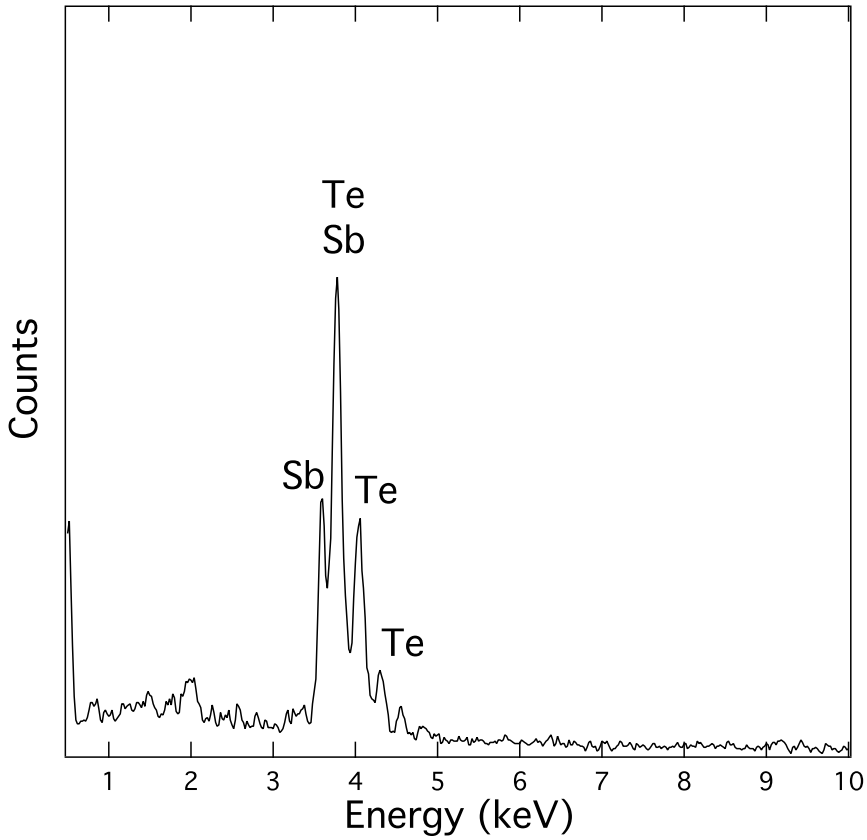

Figure 3.7: Representative EDS spectra of antimony telluride nanowires.

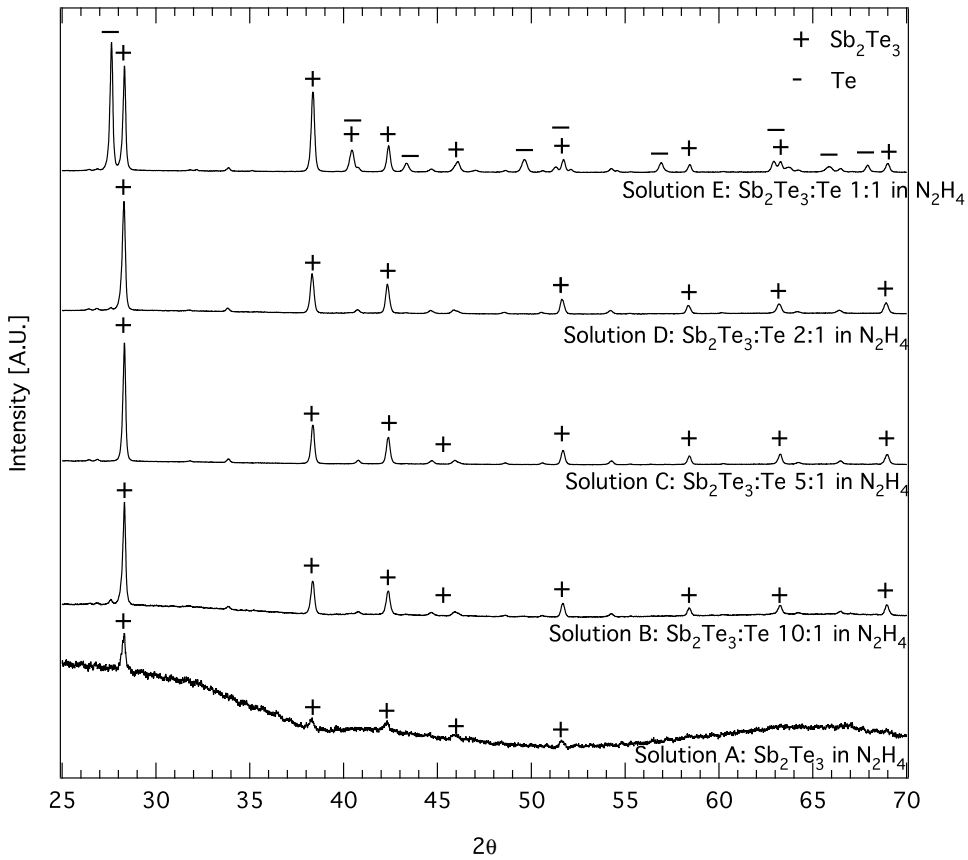

Figure 3.8: Powder X-ray diffraction of annealed arrays of nanowires before being released from alumina templates from precursor solutions of $Sb_2Te_3/Te/N_2H_4$.

3.4 Antimony Telluride Thin Films via Evaporation

Antimony telluride thin films were fabricated by controlled evaporation of the precursor on silicon dioxide surfaces. Thin films were grown on silicon wafers with 250 nm of thermally grown silicon dioxide on the wafer surface to ensure an insulating surface suitable for electrical conductivity measurements of the film. Substrates were held normal to the precursor solution surface. As the solvent slowly evaporates, a thin film is deposited onto the substrate. Annealing of the precursor coated substrate in an inert atmosphere completes thin film formation. This simple method of producing antimony telluride thin films does not require special conditions such as high vacuum and is low-cost and high-throughput. The film geometry also allows for the measurement of thermoelectric properties such as electrical conductivity and thermoelectric power.

The morphology of the thin films was investigated by differential contrast interference (DIC) microscopy, SEM, and profilometry. DIC microscopy provides a very wide lateral view while being very sensitive (on the order of nanometers) to changes in topography of the surface. DIC images (Figure 3.9) show films that have good continuous coverage of the substrate over micron areas with a rough surface. SEM images of the films (Figure 3.10) show the films rough morphology and continuity on a smaller length scale.

Electrical conductivity and thermoelectric power measurements of the films obtained from precursor solution A (Sb_2Te_3 in hydrazine) and solution E (1:1 Sb_2Te_3:Te in hydrazine) were completed (Table 3.2). Square areas of the film ($\sim 1 \times 1$ cm) were fabricated via simple masking and etching. In order to make good ohmic contact between the electrodes and the film, small nickel pads were evaporated in each of the four corners of the square film. I-V curves for the films show good

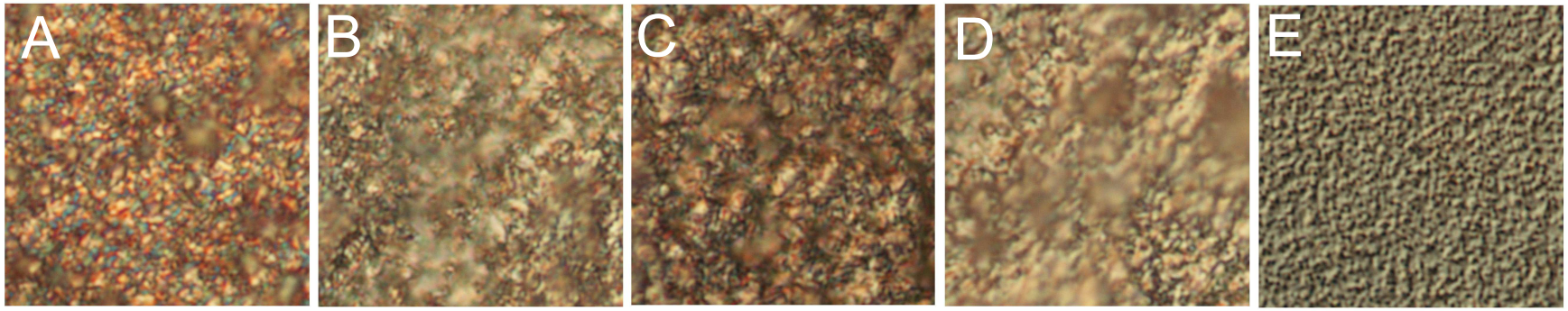

Figure 3.9: Optical microscopy DIC images of thin films obtained from solutions A–E.

ohmic behavior (Figure 3.11). The sheet resistance was calculated via the Van der Pauw method.[23] Film thickness was determined by profilometry measurements to determine the electrical conductivity. Films from precursor A were thinner (2.2 μm) than films from precursor E (5.2 μm), which is likely due to the higher concentration of precursor in solution E. Films A and E have reasonable electrical conductivities of 44 $S\,cm^{-1}$ and 65 $S\,cm^{-1}$, respectively. Films A and E also have reasonable thermoelectric powers of 73 $\mu V\,K^{-1}$ and −53 $\mu V\,K^{-1}$, respectively. This compared to an electrical conductivity of ∼500 $S\,cm^{-1}$ and a thermoelectric power ∼153 $\mu V\,K^{-1}$ for ∼1 μm thick Sb_2Te_3 films prepared by vacuum deposition.[7] Film E has a negative thermoelectric power that is presumably due to n-type doping due to the presence of a pure tellurium phase in the film. (See Figure 3.12). Being able to fabricate both n-type and p-type films using the same method is also attractive for thermoelectric element construction, where both p-type and n-type materials are required. The evaporated films described in this chapter show lower electrical conductivities and thermoelectric power; however, the method by which the evaporated films are made is very simple and requires no high-vacuum deposition chamber. Further optimization of the deposition procedure could lead to better performing films.

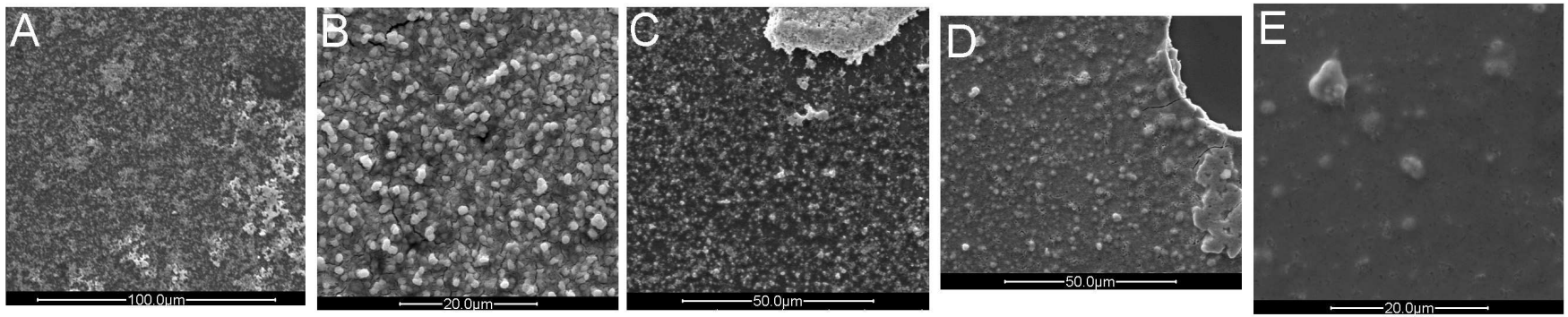

Figure 3.10: FESEM images of thin films obtained from solutions A–E.

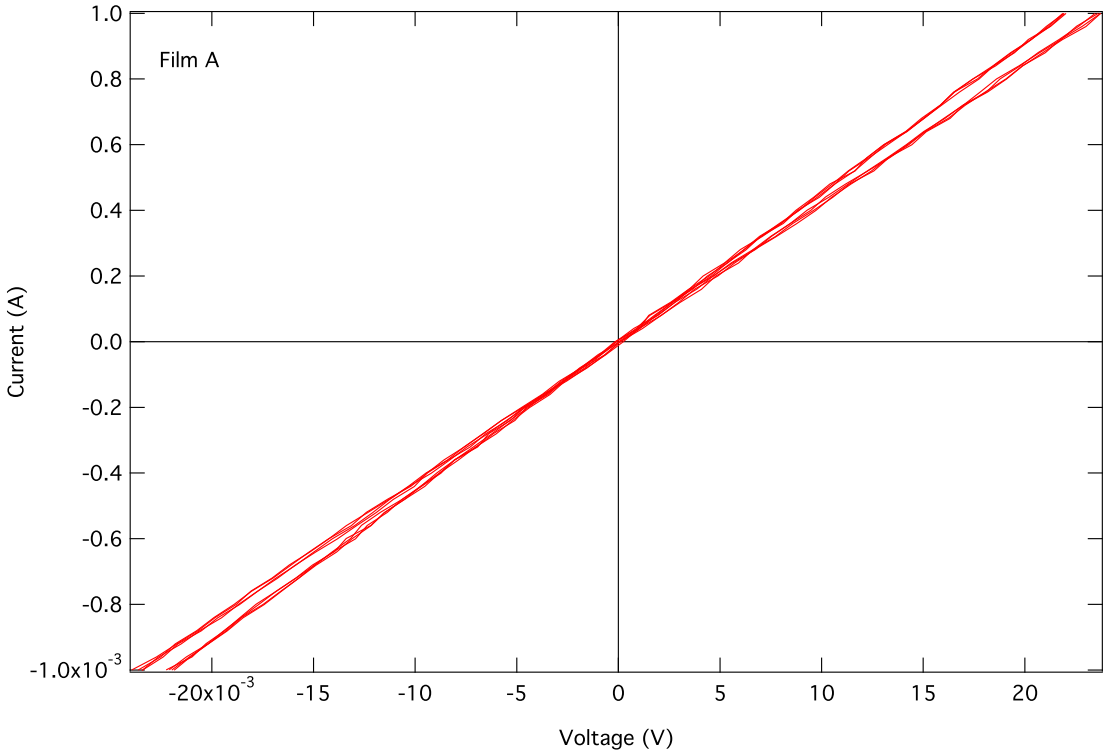

Figure 3.11: I-V characteristics of an evaporated thin film obtained from solution A.

Table 3.2: Electronic properties of antimony telluride thin films prepared via hydrazine method compared to a vacuum deposited thin film.

Sample ID	Film thickness (μm)	σ ($S\,cm^{-1}$)	S ($\mu V\,K^{-1}$)
Film A	2.2	44	73
Film E	5.2	65	−53
Vacuum deposited film[a]	∼ 1	∼ 500	∼ 153

[a] Gonclaves, L.; Alpuim, P.; Min, G.; Rowe, D.; Couto, C.; Correia, J. *Vacuum* **2008**, *82*, 1499–1502.

The composition of the thin films was investigated via powder XRD and EDS. EDS spectra of the thin films show peaks for both antimony and tellurium (Figure 3.13). A comparison of the EDS spectra of the two films suggests film E is slightly enriched with tellurium. Similarly to powder XRD patterns of annealed nanowire samples, powder XRD of the films show that film A is composed of rhombohedral antimony telluride, with a small amount of tellurium present in the film (Figure 3.12). Film E shows a composite material of antimony telluride and tellurium. The presence of a tellurium phase in film E also explains the negative thermoelectric power observed in this sample.

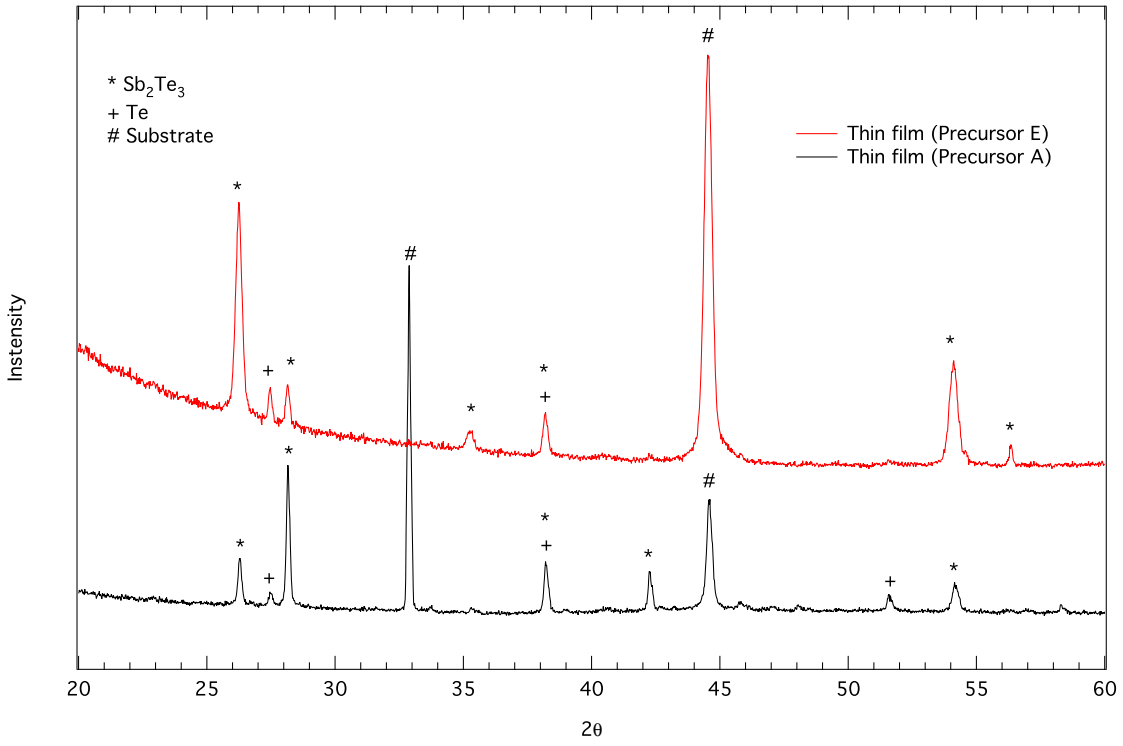

Figure 3.12: Powder X-ray diffraction of thin films obtained from solutions A and E.

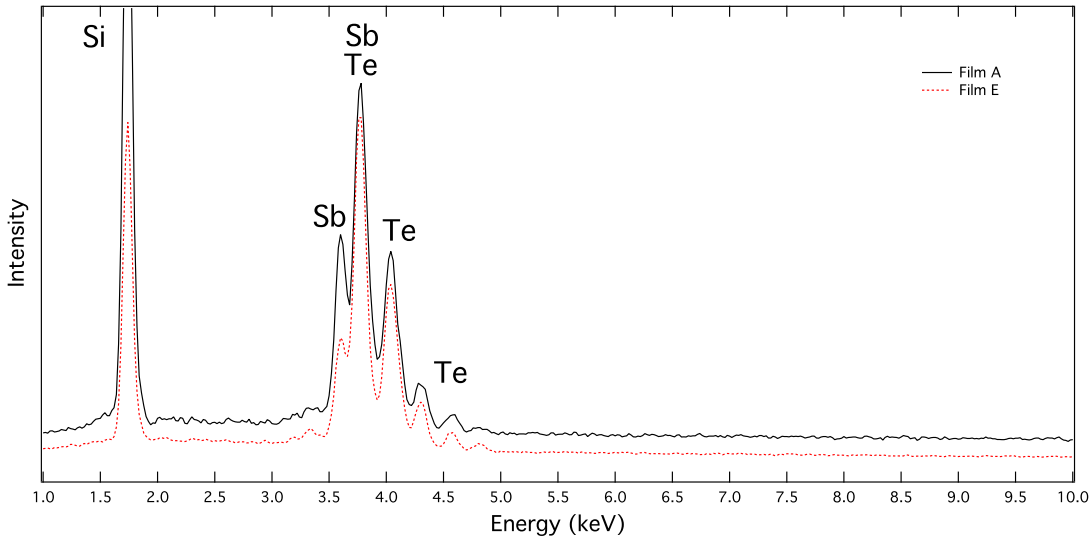

Figure 3.13: Representative EDS spectra of antimony telluride thin films.

3.5 Conclusions

The reducing and coordinating properties of hydrazine make it a versatile solvent for the dissolution of semiconductor chalcogenides. This has been proven in the case of antimony telluride. By adding small amounts of tellurium, the solubility of antimony telluride in hydrazine is greatly enhanced. Solutions of antimony telluride and tellurium in hydrazine were utilized to fabricate antimony telluride and antimony telluride/tellurium composite nanowires and thin films through very simple and effective templating methods. Thermoelectric properties measurements conducted on antimony telluride and antimony telluride/tellurium thin films show promising results for this method.

3.6 Experimental

A typical preparation of an antimony telluride precursor is decribed: under an inert atmosphere a solution of 0.225 mmol of antimony telluride (99.99%) is added to 3 mL of anhydrous hydrazine (98%) and stirred for 10 days. The previously clear solution became a deep red-orange solution after a few days. This solution is then filtered through a 0.20 μm syringe filter before using it to fabricate nanowires or thin films.

Nanowires are fabricated by slowly adding a precursor solution to an alumina template. The solution is added dropwise (30 μL at a time for a total of 210 μL) to a commercially obtained alumina template with a pore size of 200 nm. The solvent is allowed to evaporate over a period of 24 h. The alumina template is then placed in a furnace and heated to 400 °C for 24 h under the flow of nitrogen. The nanowires are then released from the membrane by selectively dissolving the alumina membrane in a 3 M NaOH solution. Nanowires are then rinsed three times each, with 3 M NaOH, deionized water, and ethanol, with separation by centrifugation between each rinse.

Antimony telluride thin films are fabricated on silicon wafers which have 250 nm of silcon dioxide thermally grown on the surface. Wafers are cleaned thoroughly in hot (100 °C) piranha solution (4:1 v/v ratio of concentrated sulfuric acid to 30% hydrogen peroxide). Wafers are rinsed with deionized water and thoroughly dried under a stream of nitrogen. Under an inert atmostphere, wafers are suspended in an antimony telluride precursor solution with the substrate surface normal to the solution surface. The solution is allowed to evaporate over a period of days. Films are annealed at 400 °C under an inert atmosphere for 24 hours.

Powder XRD patterns were taken with a Rigaku (RU-200) high-brilliance X-ray

generator equipped with a Guinier camera (G670 from Huber Diffraktiontechnik GmbH & Co. KG) using monochromatized Cu Kα (λ = 1.5418 Å) radiation. TEM micrographs were recorded on a JEOL 2010 LaB6 instrument operating at 200 kV. FESEM micrographs were recorded on a JEOL 6700F operating at 3 kV. ESEM micrographs were recorded on a FEI Quanta 200 ESEM. Reflected differential interference constrast (DIC) images were taken using an olympus bx62 microscope with a 100× objective. Thermoelectric power measurements were made using a reported in-house instrument.[24] Electrical conductivity was calculated by measuring the sample dimension and sheet resistance using the four-probe technique and Van der Pauw method. Thermal studies were conducted using a DSC (TA Instruments 2420) and TGA (TA instruments Q600) at a heating rate of 10 °C min^{-1} under argon.

3.7 References

[1] Wang, W.; Yan, X.; Poudel, B.; Ma, Y.; Hao, Q.; Yang, J.; Chen, G.; Ren, Z. *J. Nanosci. Nanotechno.* **2008**, *8*, 452–456.

[2] Wang, Q.; Jiang, C.; Yu, C.; Chen, Q. *J. Nanopart. Res.* **2007**, *9*, 269–274.

[3] Meister, S.; Peng, H.; McIIwrath, K.; Jarausch,; K. Zhang, X.; Cui, Y. *Nano. Lett.* **2006**, *7*, 1514–1517.

[4] Jin, C.; Zhang, G.; Qian, T.; Li, X.; Yao, Z. *J. Phys. Chem. B.* **2005**, *109*, 1430–1432.

[5] Lee, J.; Brittman, S.; Yu, D.; Park, H. *J. Am. Chem. Soc.* **2008**, *130*, 6252–6258.

[6] Huang, Q.; Kellock, A.; Raoux, S. *J. Electrochem. Soc.* **2008**, *155*, D104–D109.

[7] Gonclaves, L.; Alpuim, P.; Min, G.; Rowe, D.; Couto, C.; Correia, J. *Vacuum* **2008**, *82*, 1499–1502.

[8] Cepak, V.; Martin, C. *Chem. Mater.* **1999**, *11*, 1363–1367.

[9] Martin, C. *Chem. Mater.* **1996**, *8*, 1739.

[10] Mitzi, D. *J. Mater. Chem.* **2004**, *14*, 2355–2365.

[11] Mitzi, D. *Inorg. Chem.* **2005**, *44*, 3755–3761.

[12] Mitzi, D. *Inorg. Chem.* **2005**, *44*, 7078–7086.

[13] Mitzi, D.; Copel, M.; Murray, C. *Adv. Mater.* **2006**, *18*, 2448–2452.

[14] Mitzi, D.; Copel, M.; Chey, S. *Adv. Mater.* **2005**, *17*, 1285–1289.

[15] Mitzi, D.; Yuan, M.; Liu, W.; Kellock, A.; Chey, S.; Deline, V.; Schrott, A. *Adv. Mater.* **2008**, *20*, 3657–3662.

[16] Mitzi, D.; Kosbar, L.; Murray, C.; Copel, M.; Afzali, A. *Nature* **2004**, *18*, 299–303.

[17] Lucien, H. *J. Chem. Eng. Data* **1961**, *6*, 584–586.

[18] Milliron, D.; Mitzi, D.; Copel, M.; Murray, C. *Chem. Mater.* **2006**, *18*, 587–590.

[19] Zou, H.; Rowe, D.; Williams, S. *Thin Solid Films* **2002**, *408*, 270–274.

[20] Feutelais, Y.; Legendre, B. *Thermochim. Acta* **1998**, *314*, 35–53.

[21] Hochbaum, A.; Chen, R.; Delgado, R.; Liang, W.; Garnett, E.; Najarian, M.; Majumdar, A.; Yang, P. *Nature* **2008**, *451*, 163–167.

[22] Scherrer, H.; Scherrer, S. *Thermoelectrics Handbook Macro to Nano*; Taylor and Francis, 2006; Vol. 2, p 6 ch. 27.

[23] Van der Pauw, J. *Philips Res. Reps.* **1958**, *13*, 1–9.

[24] Polvani, D.; Meng, J.; Hasegawa, M.; Badding, J. *Rev. Sci. Instr.* **1999**, *70*, 3586–3589.

Chapter Four

Polytetrafluoroethylene Palladium and Iron Nanocomposites via Jet Blowing

4.1 Introduction

Polymer/metal nanocomposites find a variety of applications ranging from catalysis, magnetic materials to optoelectronics.[1–3] Unique features like high strength, light weight, and comparatively low cost make polymer nanocomposites suitable candidates for the replacement of metals in automobile and aerospace industries. It is estimated that widespread use of polymer nanocomposites (PNCs) by car manufacturers could save over 1.5 billion liters of gasoline annually and reduce CO_2 emissions by nearly 10 billion pounds.[3]

Polytetrafluoroethylene (PTFE) is a fluoropolymer commonly known for its exceptional properties such as high thermal stability, hydrophobicity, and chemical resistance. However, these properties also make the processing of PTFE more laborious and tedious.[4] The most commonly employed processing techniques for PTFE are similar to those used for powder metallurgy and involve multiple steps followed by stretching and/or sintering.[4 5] The work reported in this chapter represents an extension of the "jet blowing" process we have developed in our lab. Jet blowing is an environmentally friendly, single step, solvent-free technique to process pure ultra-high molecular weight PTFE at temperatures even below its melting point into micro- and nanofibers up to 3 or 4 mm long inside of a high pressure jet of gases such as nitrogen or argon.[6] Jet blowing allows for the fabrication of PTFE fibers that can be produced in large quantities at a rapid rate and will adhere to many different materials, allowing for facile fabrication of surface modifying coatings and dense fiber mats.

The most common approach to make PNCs involves blending of presynthesized metal nanoparticles with the polymer either in solution or in the melt.[7–9] This technique has several disadvantages such as the need to presynthesize nano-

materials, aggregation of nanoparticles, and localized dispersion of particles. Furthermore in case of PTFE, the high melting transition, melt viscosity, and poor solubility of PTFE in common organic solvents make blending of presynthesized nanoparticles a great challenege. Previously reported examples of PTFE nanocomposites include incorporating alumina,[10] gold[11] and iron nanoparticles,[12] and carbon nanotubes.[13] Nanoparticulate alumina and carbon nanotube composites were formed through multistep mixing processes followed by hot compression molding of PTFE and prefabricated nanoparticles.[10 13] PTFE/gold nanocomposites were fabricated via high vacuum deposition and plasma treatment.[11] Previously reported PTFE/iron nanocomposites were fabricated via high-energy ball milling of PTFE and iron, which resulted in the formation of several iron fluoride phases.[12] In contrast, the jet blowing method is a simple, single step method to produce PTFE/metal nanocomposites without using prefabricated nanoparticles, high vacuum, or high-energy ball milling. In addition, the method by which PTFE is impregnated with metal nanoparticles can easily be extended to other metals.

Polytetrafluoroethylene/iron or palladium nanocomposites are synthesized in situ by decomposition of the appropriate metal acetate in presence of PTFE. The jet blowing of this mixture results in PTFE nano/micro fibers with metal nanoparticles impregnated in PTFE matrix. TEM analyses of the ultrathin, cryotomed thin films of the fiber mats shows the formation of metal nanoparticles of 20–50 nm in diameter with a uniform dispersion in the polymer matrix. Thermogravimetric analysis of the jet blown fibers showed significant residue left and is proportional with the amount of metal acetate used in the feed material.

4.2 Fabrication of Polytetrafluoroethylene Palladium and Iron Nanocomposites

The synthesis of iron and palladium nanoparticles in a PTFE matrix was performed by stirring the respective metal acetates with PTFE powder in chloroform solution for 16 hours. The chloroform was removed completely and the mixture was then heated above the decomposition temperature of metal acetate under a continuous flow of nitrogen gas. After decomposition the PTFE/Pd matrix turns black and the PTFE/Fe matrix turns to brick red color, suggesting complete decomposition of corresponding metal acetate to the metal. Two different compositions of polymer to metal acetate ratio have been prepared, 10% and 15% (w/w) metal acetate. These mixtures were then jet blown at 310 °C using nitrogen gas. It was observed that the pressure required for jet blowing of the composite material was higher than that for PTFE. The jet blowing for PTFE under similar conditions also results in fibers (Figure 4.1) with similar dimensions but requires much lower pressures. This suggests that the nanoparticles have a reinforcing effect in the pre-jet blown material.

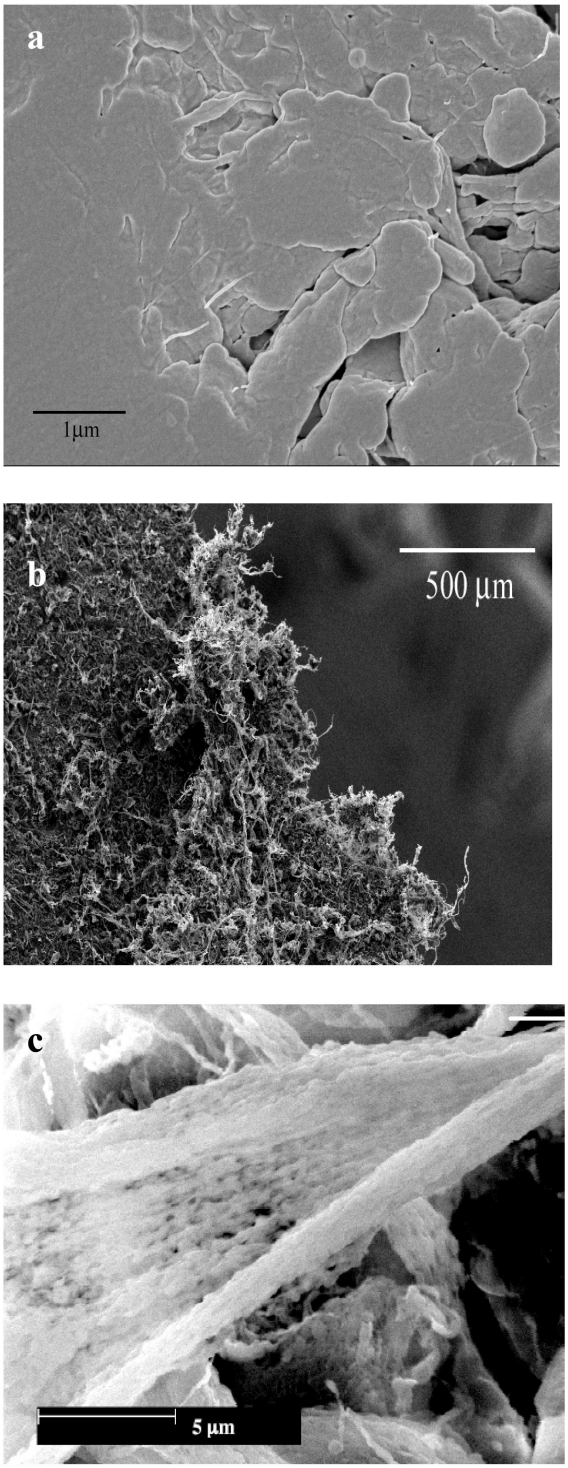

Figure 4.1: Electron microscope images of A: pre-jet blown PTFE 7A B: Low magnification image of jet blown PTFE 7A at 310℃ using nitrogen gas, and C: High magnification image of jet blown PTFE 7A310℃ using nitrogen gas.

4.3 Characterization of Polytetrafluoroethylene Palladium and Iron Nanocomposites

The thermal stability of the iron and palladium composite materials was investigated by thermogravimetry (TGA) and compared to those of PTFE jet blown under similar conditions (Figure 4.2). Pure jet blown PTFE leaves very little residue when heated to 650 °C (0.8%). There is a significant amount of nonvolatile residue left when the composite material is heated, presumably due to the presence of metal nanoparticles. Moreover, as expected, the amount of residue is proportional to the amount of metal acetate added prior to jet blowing and it increases with increase in amount of metal acetate in the feed.

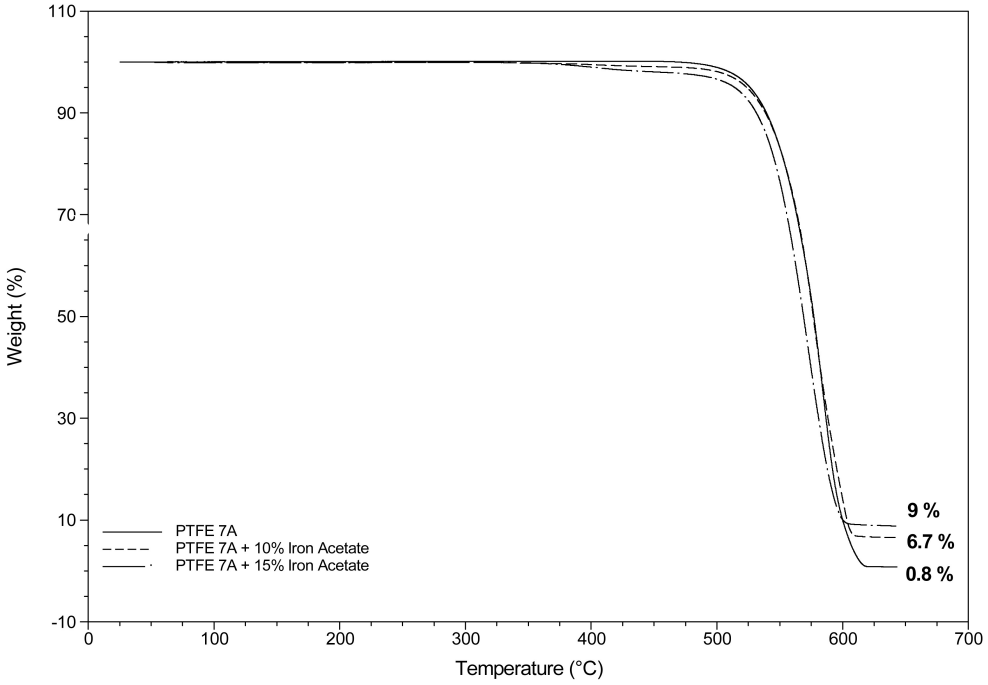

Figure 4.2: TGA of virgin PTFE7A, annealed 15% iron acetate/PTFE mixture, and annealed 10% iron acetate/PTFE mixture.

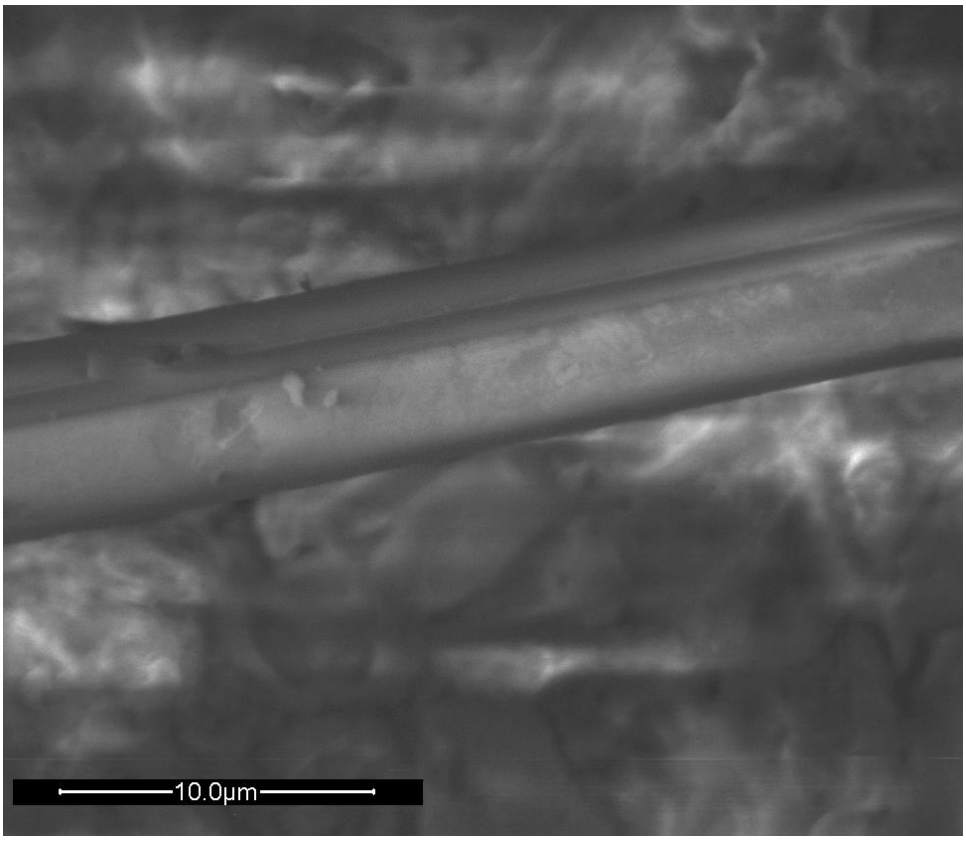

Figure 4.3: Electron microscope image of a jet blown PTFE/iron nanocomposite from 10% iron acetate/PTFE mixture.

SEM analysis of jet blown composite shows the fibrous nature of the material (Figure 4.3); however, it was difficult to detect the incorporated metal nanoparticles as the PTFE matrix surrounds them. EDS analysis of the fibers show low intensity peak for both Pd and Fe, indicating that the metal nanoparticles are encapsulated in the PTFE matrix. Therefore, the nanofibrous composite materials were sectioned under ultrathin cryotomy into thin films. In order to get uniform sections, ultrathin cryotomy was carried out with freshly cleaved glass knives at ∼−110 °C, well below the conventional glass transition temperature of PTFE (−85 °C). Figures 4.4 and 4.5 show TEM images of palladium and iron nanoparticles and their EDS spectra, respectively. In both the composites, the EDS analysis shows an intense peak for Fe or Pd confirming the impregnation of nanoparticles in PTFE matrix. Nanoparticles approximately 20–50 nm in diameter are observed. A mixture of rod-shaped and spherical particles were observed for PTFE/iron nanocomposites, compared to spherical nanoparticles observed in PTFE/-palladium nanocomposites. The iron-containing PTFE composites are magnetic; applying a magnetic field can lift the fiber mats.

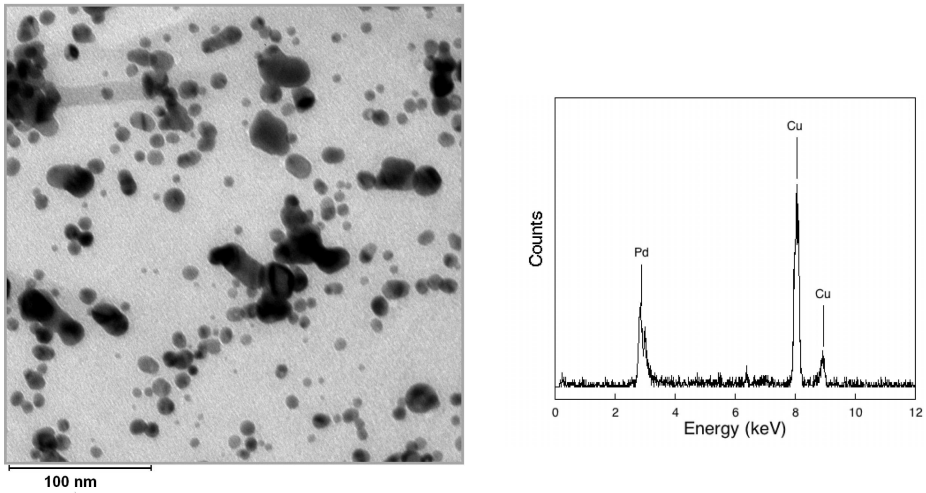

Figure 4.4: TEM image and corresponding EDS spectra of microtomed jet blown PTFE/palladium nanocomposite from 10% palladium acetate/PTFE mixture (Cu peaks in EDS due to copper support upon which the sample is mounted).

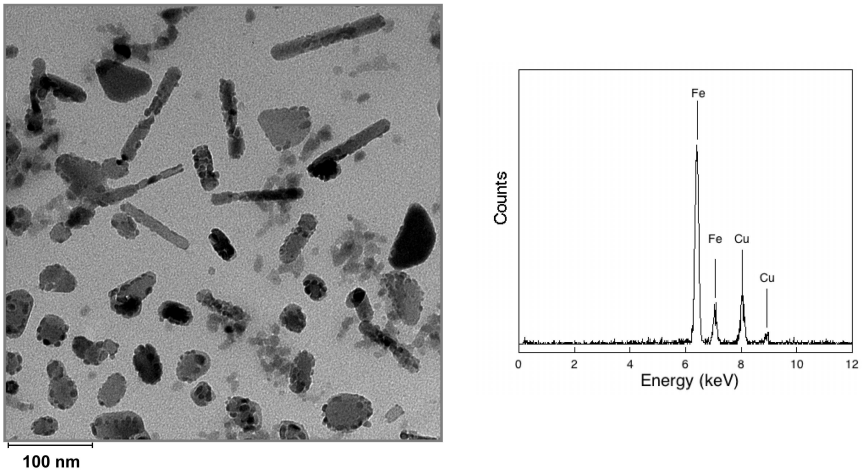

Figure 4.5: TEM image and corresponding EDS spectra of microtomed jet blown PTFE/iron nanocomposite from 10% iron acetate/PTFE mixture (Cu peaks in EDS due to copper support upon which the sample is mounted).

4.4 Conclusions

In conclusion, we have shown that PTFE/metal nanocomposites containing either iron or palladium nanoparticles can be fabricated through the simple jet blowing process. Both TGA and TEM analysis confirms the incorporation of metal nanoparticles into PTFE nano/micro fibers. Up to ~10% metal can be incorporated into the PTFE matrix. Further, the metal nanoparticles are uniformly dispersed in the PTFE fibers. Finally, the jet blowing technique allows the fabrication of previously inaccessible composites of PTFE with other materials that have potentially useful properties.

4.5 Experimental

DuPont's PTFE 7A (35–150 μm sized powder, Polyscience) and iron(II) acetate or palladium(II) acetate (Aldrich) were suspended for 16 h in chloroform with two different ratios of PTFE 7A to metal acetates: 90:10, and 85:15, w/w. The chloroform was then removed on a rotary evaporator.The PTFE/metal acetate mixtures were annealed for 6–8 h above the decomposition temperatures of the metal acetates under a flow of nitrogen gas. These mixtures were then jet blown at 310 °C using high pressure nitrogen (~100 MPa): 0.5 g of the mixture was loaded into a $\frac{1}{4}''$ ID stainless steel tube capable of containing 270 MPa. A stainless steel nozzle with a $\frac{1}{16}''$ opening terminated by a capillary opening of 50–150 μm in diameter and 0.5-2 mm long was connected to the stainless steel tube via a commercial high pressure coupling. The assembly was heated to the desired jet blowing temperature of 310 °C. A valve was opened to allow high pressure argon or nitrogen into the preheated stainless steel tube to initiate the jet blowing process.

DSC and TGA analyses were performed on a TA Instruments calorimeter at a heating rate of 10 °C min^{-1}. The polymer fiber and metal nanoparticle composite thin films were sectioned by ultrathin cryotomy at −110 °C. TEM analysis of these thin films was performed by mounting them on copper grid and using JEOL JEM 1200 EXII and JEOL 2010 instruments. Low magnification SEM analyses were performed on an environmental SEM (FEI-Quanta 200) on uncoated fibers in the presence of several Torr of water vapor to prevent charging. High resolution images were collected with a field emission SEM (JEOL-6700F) after coating the samples with gold.

4.6 References

[1] Ciardelli, F.; Pertici, P.; Vitulli, G.; Giaiacopi, S.; Ruggeri, G.; Pucci, A. *Macromol. Symp.* **2006**, *231*, 125–133.

[2] Esposito, F.; Casuscelli, V.; Volpe, M. V.; Carotenuto, G.; Nicolais, L. *Polym. News* **2005**, *30*, 296–300.

[3] Heilmann, A. *Polymer Films with Embedded Metal Nanoparticles*; Springer Series in Materials Science, 2003; Vol. 52.

[4] Ebnesajjad, S. *Fluoroplastics, Volume 1: Non-Melt Processible Fluoroplastics*; Plastics Design Library, 2000; Vol. 1.

[5] Ariawan, A. B.; Ebnesajjad, S.; Hatzikiriakos, S. G. *Polym. Eng. Sci.* **2002**, *42*, 1247.

[6] Borkar, S.; Gu, B.; Dirmyer, R.; Delicado, R.; Sen, A.; Jackson, B. R.; Badding, J. V. *Polymer* **2006**, *46*, 8337–8343.

[7] Korbov, M. S.; Yurkov, G. Y.; Kozinkin, A. V.; Koksharov, Y. A.; Pirog, I. V.; Zubkov, S. V.; Kitaev, V. V.; Sarychev, D. A.; Buznik, V. M.; Tsvetnikov, A. K.; Gubin, S. P. *Inorg. Mater.* **2004**, *40*, 26.

[8] Kozinkin, A. V.; Sever, O. V.; Gubin, S. P.; Shuvaev, A. V.; Dubovtsev, I. A. *Inorg. Mater.* **1994**, *30*, 634.

[9] Steunou, N.; Forster, S.; Florian, P.; Sanchez, C.; Antonietti, M. *J. Mater. Chem.* **2002**, *12*, 3246.

[10] Burris, D.; Sawyer, W. *Wear* **2006**, *260*, 915–918.

[11] Goncharenko, A.; Grynko, D.; Grytsenko, K.; Lozovski, V. *J. Nanosci. Nanotechno.* **2005**, *5*, 1919–1924.

[12] Qian, F.; Melhachat, B.; Chen, C.; Jiang, K.; Zhao, Z.; Yang, X. *Nucl. Sci. Tech.* **2006**, *17*, 139–142.

[13] Vail, J.; Burris, D.; Sawyer, W. *Wear* **2009**, *267*, 619–624.

Chapter Five

Conclusions

5.1 Conclusions

While significant strides in maximizing the figure of merit for thermoelectric materials have recently been made,,[1,2] the methods used to produce these materials are expensive, not amendable to scale-up for commercialization, and often require high-vacuum deposition chambers. The motivation for the research described in this thesis has been to fabricate and test thermoelectric materials by simple synthetic bench-top chemistry, which is scaleable and comparatively inexpensive. The results of the experiments described in this thesis represent significant strides in the synthesis of nanostructured thermoelecric materials and the fabrication of these nanomaterials into macroscale ensembles to measure properties relevant to thermoelectrics, such as thermoelectric power, electrical conductivity, and thermal conductivity.

In Chapter 2, the nanostructured bismuth telluride was investigated in three phases: synthesis, characterization, and measurement of thermoelectric properties of the material. Nanostructured bismuth telluride was synthesized via simple solution-based chemistry. Nanoparticle size could be tuned by adjusting reaction parameters such as length of the carbon tail of the thiol capping ligand and reaction temperature. Nanoparticle morphology, composition, surface, and thermal properties were also investigated to thoroughly characterize the material. Finally, nanoparticles were assembled into large macroscale ensembles, which allowed for characterization of the materials' thermoelectric properties. The dissolution of many semiconductors in hydrazine has been greatly employed in the fabrication of functional devices, such as thin-film transistors.[3] In Chapter 3, this method is extended to include a semiconductor that is a good thermoelectric material. The solubility of antimony telluride in hydrazine was explored with respect to the con-

centration of tellurium to aid solubility of the binary compound. Thermal properties of the soluble precursors were investigated. Antimony telluride nanowires and thin films were fabricated via simple templating methods. Thermoelectric power and electrical conductivity measurements on antimony telluride thin films show that this may be a promising processing method.

This work has important implications for the field of nanostructured thermoelectrics. It represents a starting point in the optimization of nanostructured tellurides and their fabrication into larger structures for thermoelectric properties measurements. To further improve the materials' properties, proper doping studies of the materials for both n-type and p-type thermoelectrics must be completed. Also, the assembly process of these materials from nanostructured materials into macroscale ensembles for device fabrication must also be optimized.

In Chapter 4, previously inaccessible PTFE/metal nanocomposites were fabricated through a simple procedure. Metal nanoparticles were formed in situ in the polymer matrix, which was then processed by jet blowing to form PTFE micro- and nanofibers with metal nanoparticle content as high as ~10%(w/w).

5.2 References

[1] Venkatasubramanian, R.; Siilvola, E.; Colpitts, T.; O'Quinn, B. *Nature* **2001**, *413*, 597–602.

[2] Harman, T.; Taylor, P.; Walsh, M.; LaForge, B. *Science* **2002**, *297*, 2229–2232.

[3] Mitzi, D. *J. Mater. Chem.* **2004**, *14*, 2355–2365.

Vita

Matthew Dirmyer received his Bachelors of Science degree in Chemistry with honors in 2003 from the Rochester Institute of Technology in Rochester, New York. He joined the Department of Chemistry at The Pennsylvania State University; University Park in fall of 2003 under the tutelage of Dr. Ayusman Sen. His graduate research has consisted of the synthesis, characterization, and properties measurements of materials of interest for thermoelectric applications. In the fall of 2009, he will be beginning a postdoctoral appointment at Los Alamos National Lab in New Mexico.